Documentation for the Chesapeake Bay atlas
version 2024-03-19

St-Laurent, P., M.A.M. Friedrichs
Virginia Institute of Marine Science
Contact: pst-laurent@vims.edu

Contents

1 Introduction

Over the past four decades, the monitoring programs of the Chesapeake Bay have contributed to making this coastal ecosystem one of the most data-rich in the world. This continuous data collection simultaneously allowed for the development and calibration of increasingly capable 3D hydrodynamical-biogeochemical models of the estuary. Such models have the advantages of: (a) integrating the environmental variables into a cohesive whole, (b) extrapolating these variables across time, depths, and locations throughout the Bay, and (c) providing additional variables that are never sampled or had their sampling discontinued. These capabilities of models are exploited here to generate a climatological atlas of conditions in the Chesapeake Bay based on a 1985–2023 hindcast simulation with ROMS-ECB (see §5). This particular model has been in continuous development at the Virginia Institute of Marine Science (VIMS) over the past 10 years and is the backbone of the Chesapeake Bay Environmental Forecasting system (CBEFS, www.vims.edu/cbefs).

The variables featured in the atlas (see the next sections) are available as a monthly climatology representative of 1985–2023 for the surface and the bottom of the water column at a horizontal resolution of 0.00684° of longitude by 0.00540° of latitude ($\approx 600\,\mathrm{m} \times 600\,\mathrm{m}$). The atlas is distributed in a NetCDF archive (atlas_chesbay_vyyyymmdd.nc, the date yyyymmdd indicating the atlas' version) that can be visualized in QGIS/ArcGIS, Python, R, Matlab or Octave (§4). The present document provides background information as well as selected visualizations.

The atlas can serve as a baseline for the Bay against which year-to-year variability or long-term changes (such as coastal acidification) can be assessed. The model on which the atlas is based (ROMS-ECB) is operated in a free-running mode (*i.e.*, no data assimilation; see §5) and an evaluation of its skill is provided in §6.

2 Variables included in the atlas

Name	NetCDF variable(s)	units
Topography	`topography`, `mask_land_sea`	m NAVD88
Tidal range	`tidal_range`	m
Wind velocity	`wind_velocity`	m s^{-1}
Dir. wind is blowing to	`wind_direction`	°ccw from east
Significant wave height	`sig_wave_height`	m
Sea surface height	`sea_surface_height`	m NAVD88
Horizontal currents	`u_surface`,`v_surface`,`u_bottom`,`v_bottom`	m s^{-1}
Bottom stress	`stress_bottom`	Pascal
Potential temperature	`temperature_surface`,`temperature_bottom`	°C
Practical salinity	`salinity_surface`,`salinity_bottom`	–
Vertical diffusivity	`vdiff_surface`,`vdiff_bottom`	m^2 s^{-1}
Inorg. Susp. Solids (ISS)	`ISS_surface`,`ISS_bottom`	mg L^{-1}
Total Susp. Solids (TSS)	`TSS_surface`,`TSS_bottom`	mg L^{-1}
Diffuse light atten. (K_d)	`kd_surface`	m^{-1}
Dissolved dioxygen (O_2)	`O2_surface`,`O2_bottom`	mg-O_2 L^{-1}
Diss. Inorg. Nitr. (DIN)	`DIN_surface`,`DIN_bottom`	mg-N L^{-1}
Diss. Org. Nitr. (DON)	`DON_surface`,`DON_bottom`	mg-N L^{-1}
Part. Org. Nitr. (PON)	`PON_surface`,`PON_bottom`	mg-N L^{-1}
Diss. Org. Carb. (DOC)	`DOC_surface`,`DOC_bottom`	mg-C L^{-1}
Part. Org. Carb. (POC)	`POC_surface`,`POC_bottom`	mg-C L^{-1}
Total Alkalinity (TA)	`TA_surface`,`TA_bottom`	μmol kg^{-1}
Diss. Inorg. Carb. (DIC)	`DIC_surface`,`DIC_bottom`	μmol-C kg^{-1}
Dissolved calcium	`calcium_surface`,`calcium_bottom`	μmol-Ca kg^{-1}
Potential Hydrogen (pH)	`pH_surface`,`pH_bottom`	Total scale
Part. press. CO_2 (pCO_2)	`pCO2_surface`,`pCO2_bottom`	μatm
Calcite sat. state (Ω_{Ca})	`Omega_ca_surface`,`Omega_ca_bottom`	–
Arag. sat. state (Ω_{Ar})	`Omega_ar_surface`,`Omega_ar_bottom`	–

3 Notes about selected variables

The **Topography** of the model is a mosaic based on *Pope et al.* (2016), *Forte et al.* (2011), *NOAA* (2022), *National Geophysical Data Center* (1999), and *Ye et al.* (2017). The **tidal range** is computed from *Szpilka et al.* (2016) as the sum of the M_2 and S_2 water level harmonics multiplied by 2.1 ('spring tidal range', *Parker*, 2007). **Winds** at 10 m height are computed from 3-hourly snapshots of the ERA5 reanalysis (*Hersbach et al.*, 2023). The wind velocity reported in Fig. 3 is computed as $< \sqrt{u^2 + v^2} >$ (where $< . >$ denotes the temporal average over the atlas' period) while its direction is computed from `atan2`$(< v >, < u >)$. The vectors in Fig. 3 indicate the direction the wind is blowing to (not blowing from). **Significant wave height** is computed using SWAN (*Booij et al.*, 1996) and atmospheric conditions from ERA5 (the SWAN results were provided by A. Bever, AnchorQEA).

A few intertidal zones, which are areas positioned above the water level at low tide and underwater at high tide, are captured by the model: the Susquehanna flats (near Havre de Grâce, MD) and the Barrier Islands on the Atlantic side of Virginia's eastern shore (see Fig. 5). Timeseries of **sea surface height** in such intertidal zones typically exhibit a truncated sinusoidal pattern where the bottom part is clipped during the low tide portion of the cycle. As a result of this truncation, the long-term average of the timeseries results in sea surface heights that are higher inside intertidal zones compared to the rest of the Bay (Fig. 5).

Horizontal **currents** were computed by averaging the zonal (u) and meridional (v) components separately over the atlas' period. Such a long-term average removes tidal influences and reflects the mean circulation of the Bay. Note that the current's magnitude (shading) reported in Figs. 6–7 is computed as $\sqrt{< u >^2 + < v >^2}$ and is generally much slower than tidal currents at flow/ebb tide. **Bottom stress** on the other hand was computed as $< \sqrt{\tau_u^2 + \tau_v^2} >$ and therefore includes the contribution from tides.

Potential temperature in shallow environments such as the Chesapeake Bay is largely undistinguishable from the *in situ* temperature measured by an instrument. The two can be used interchangeably in this context. The atlas uses potential temperature because this is one of the two variables (the other being practical salinity) that form the model's equation of state.

It is customary to report **practical salinity** without units which is why Figs. 11–12 do not include units on their colorbar. Practical salinity should not be confused with *absolute salinity* as defined in the new TEOS standard of 2010 (or with older standards that predate PSS-78). Instruments sometime report a salinity unit of *psu* (practical salinity units) to prevent confusion, and psu is the same as what is presented in the atlas.

Vertical diffusivity is a variable computed by the model and represents the effect of unresolved scales of motion on mixing in the vertical direction. This parameterization is based on *Warner et al.* (2005) and the same diffusivity is used by the model for all tracers. Diffusivity is typically enhanced near the surface (as a result of winds) and near the bottom

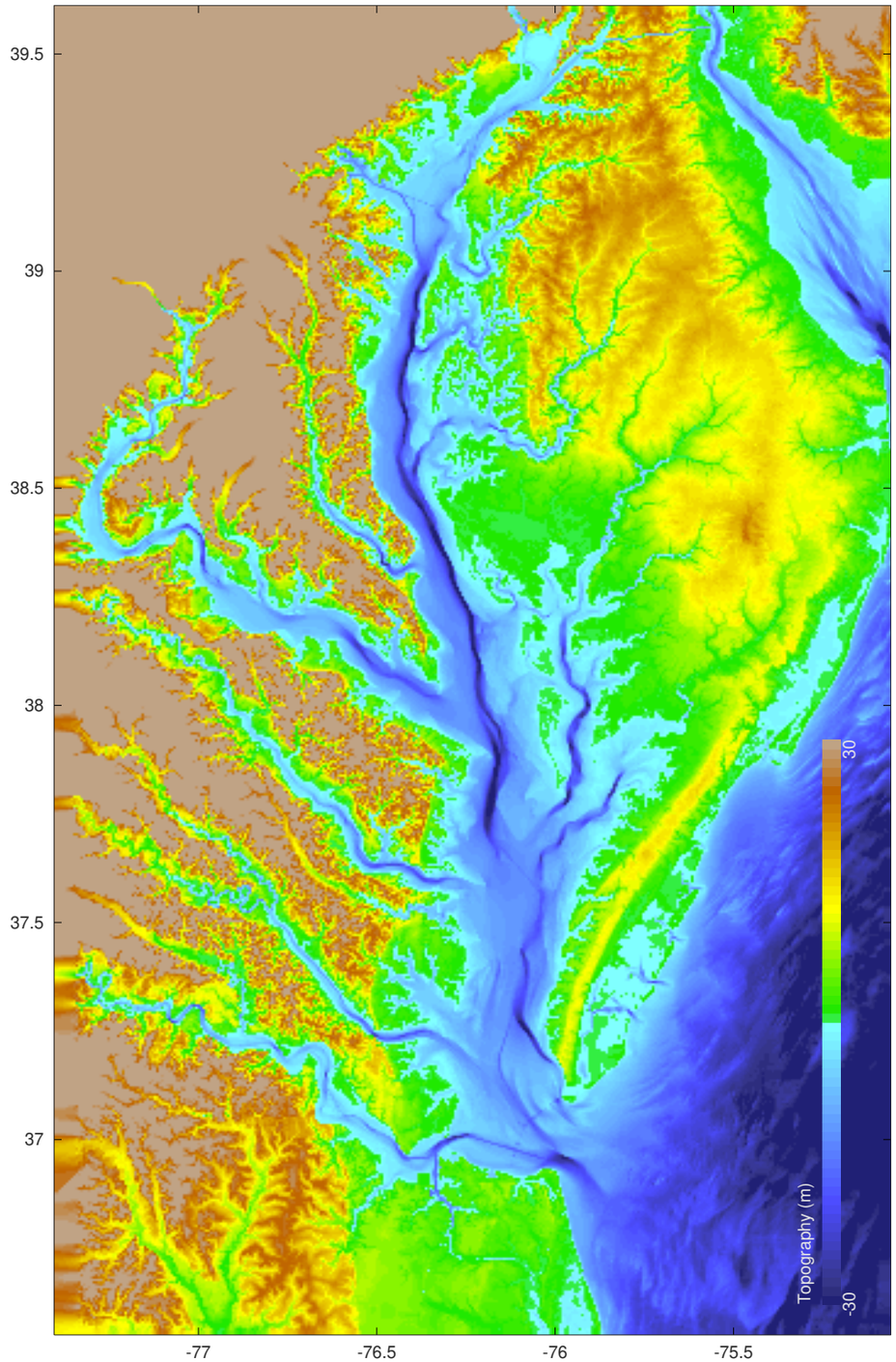

Figure 1: Topography of the Chesapeake Bay relative to NAVD88.

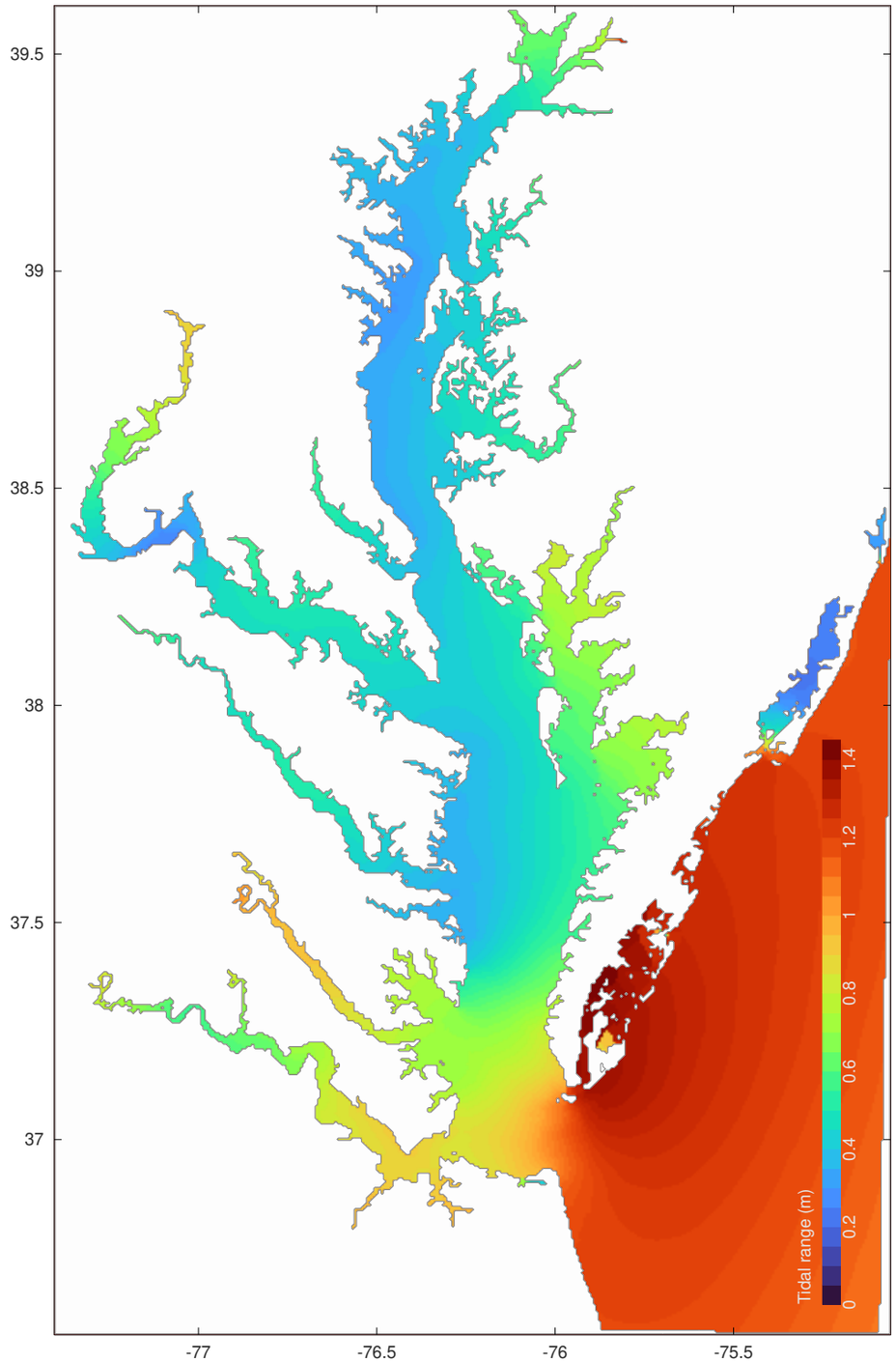

Figure 2: Tidal range.

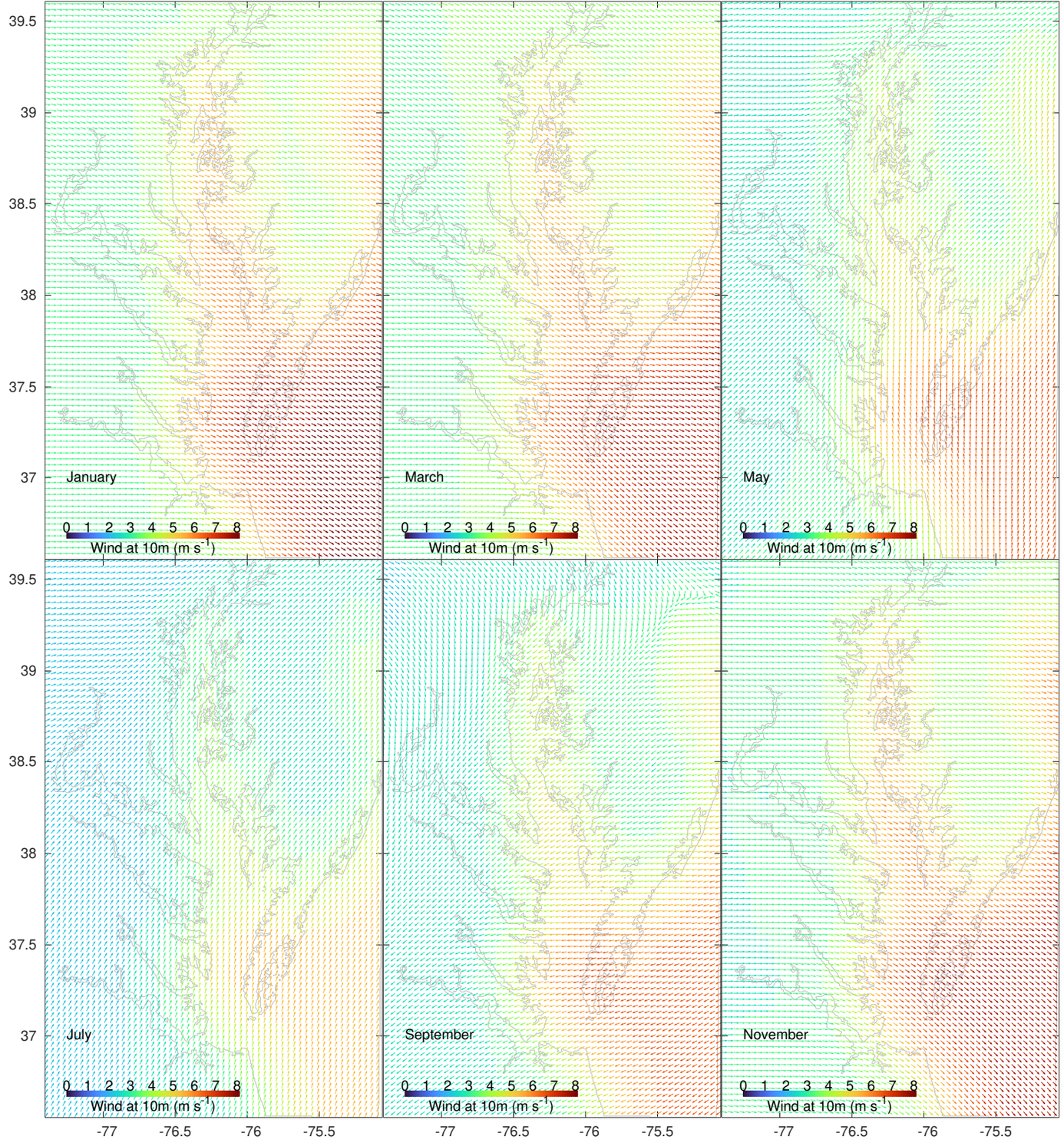

Figure 3: Winds at 10 m; only one vector out of 36 are shown for clarity. The vectors share the same length and their magnitude is indicated by the color. The arrows indicate the direction the wind is blowing toward.

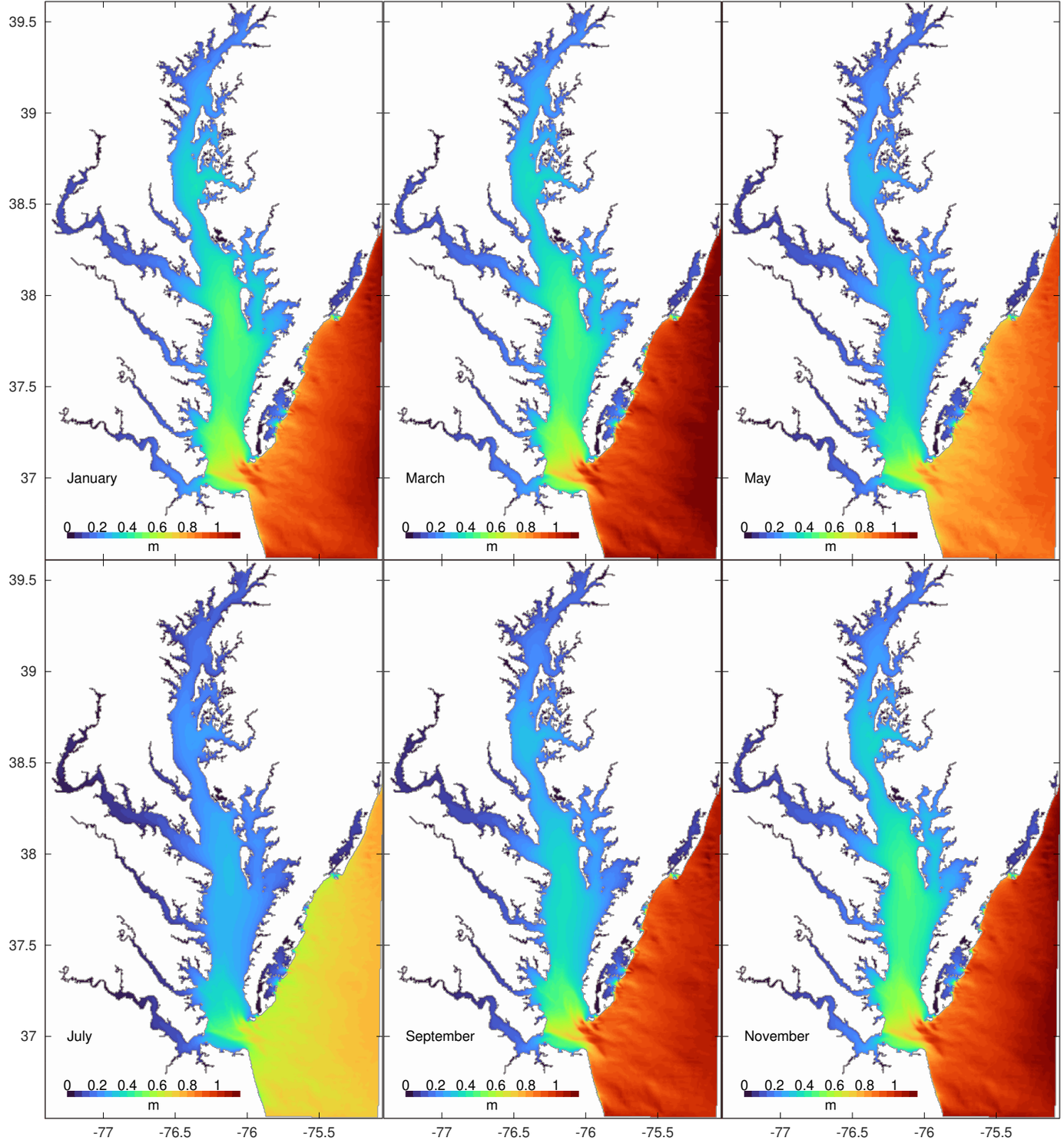

Figure 4: Significant wave height.

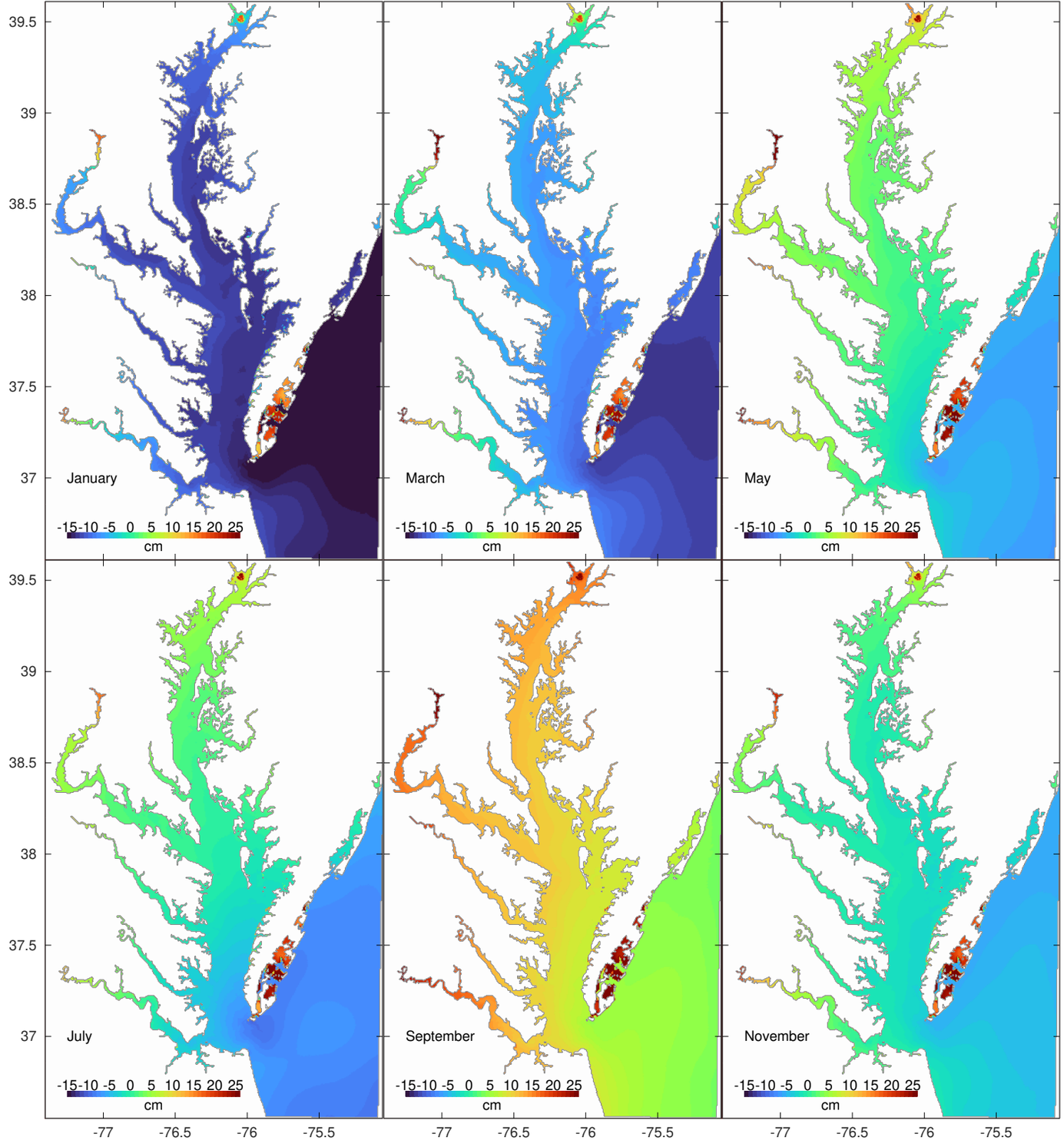

Figure 5: Sea surface height relative to NAVD88.

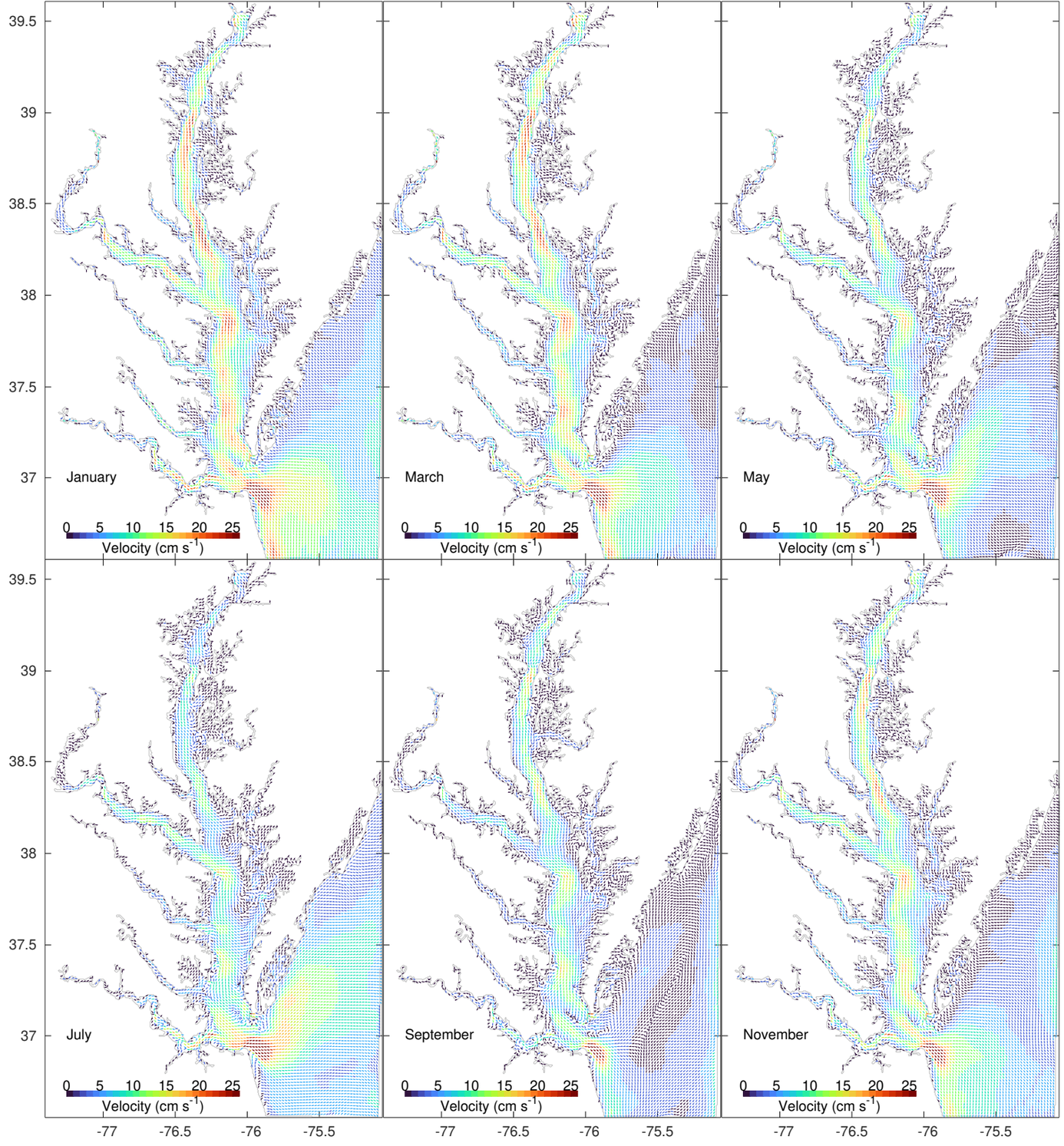

Figure 6: Horizontal currents at the surface; only one vector out of 9 are shown for clarity. The vectors share the same length and their magnitude is indicated by the color.

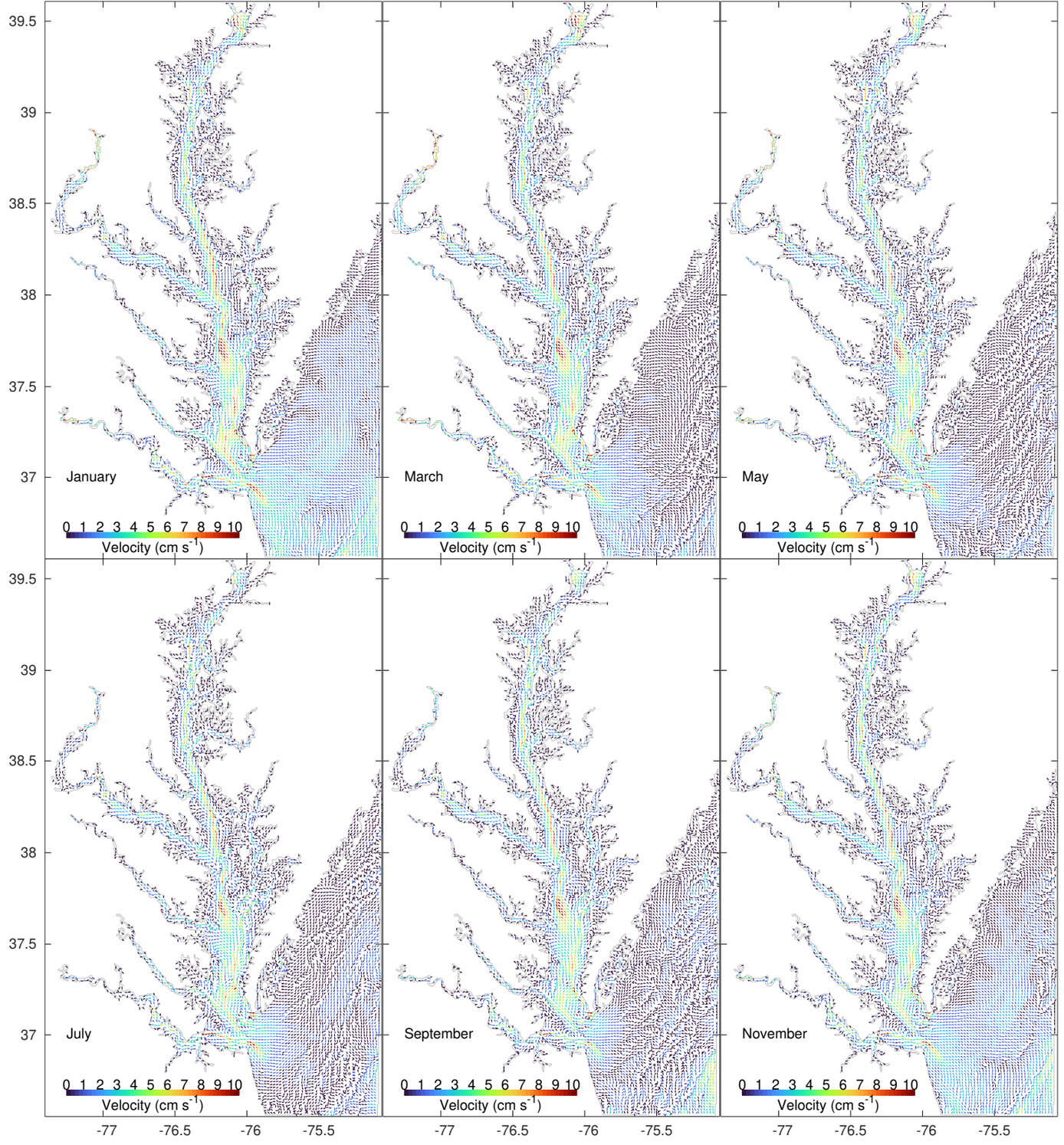

Figure 7: Horizontal currents at the bottom; only one vector out of 9 are shown for clarity. The vectors share the same length and their magnitude is indicated by the color.

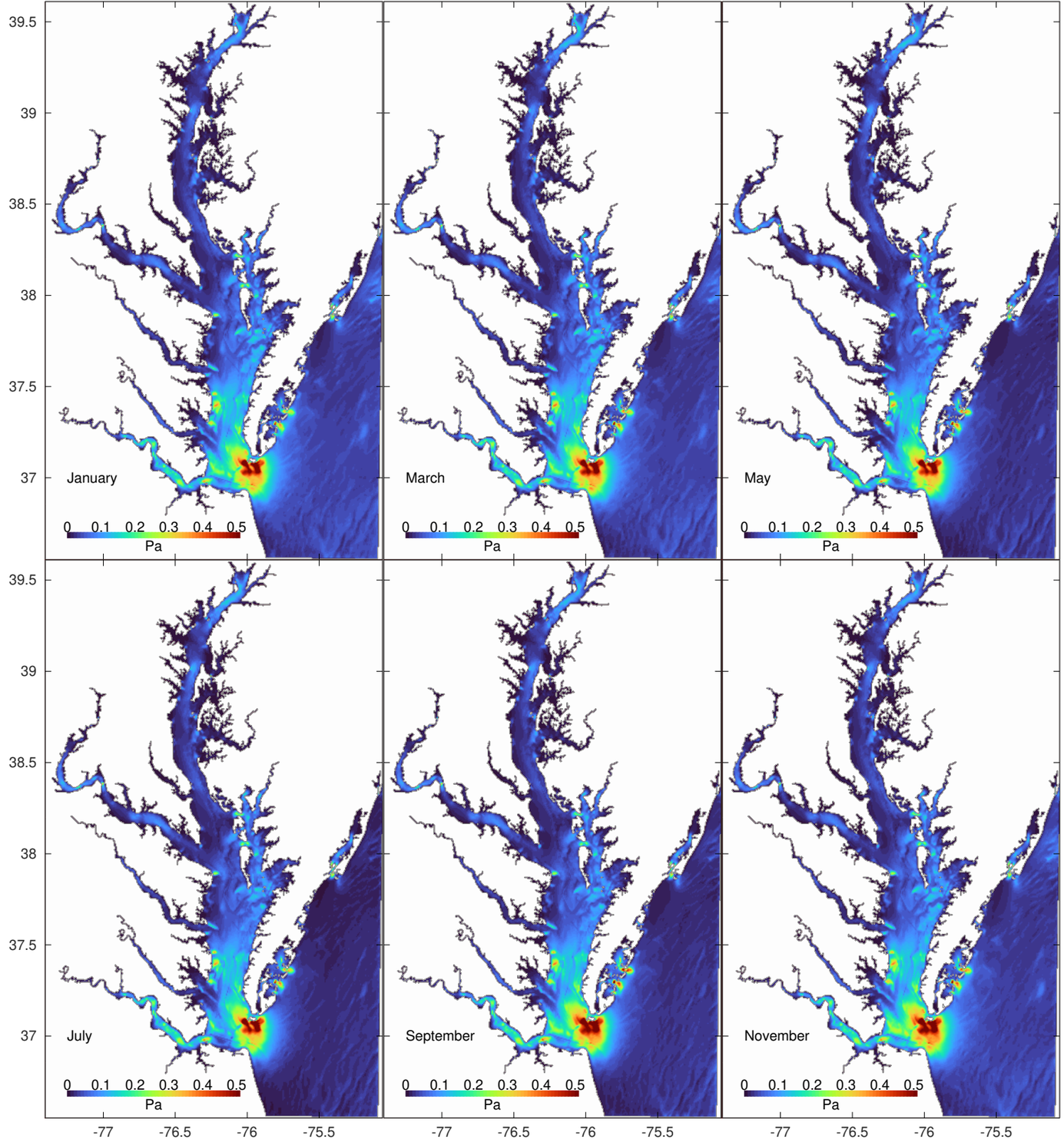

Figure 8: Stress at the bottom.

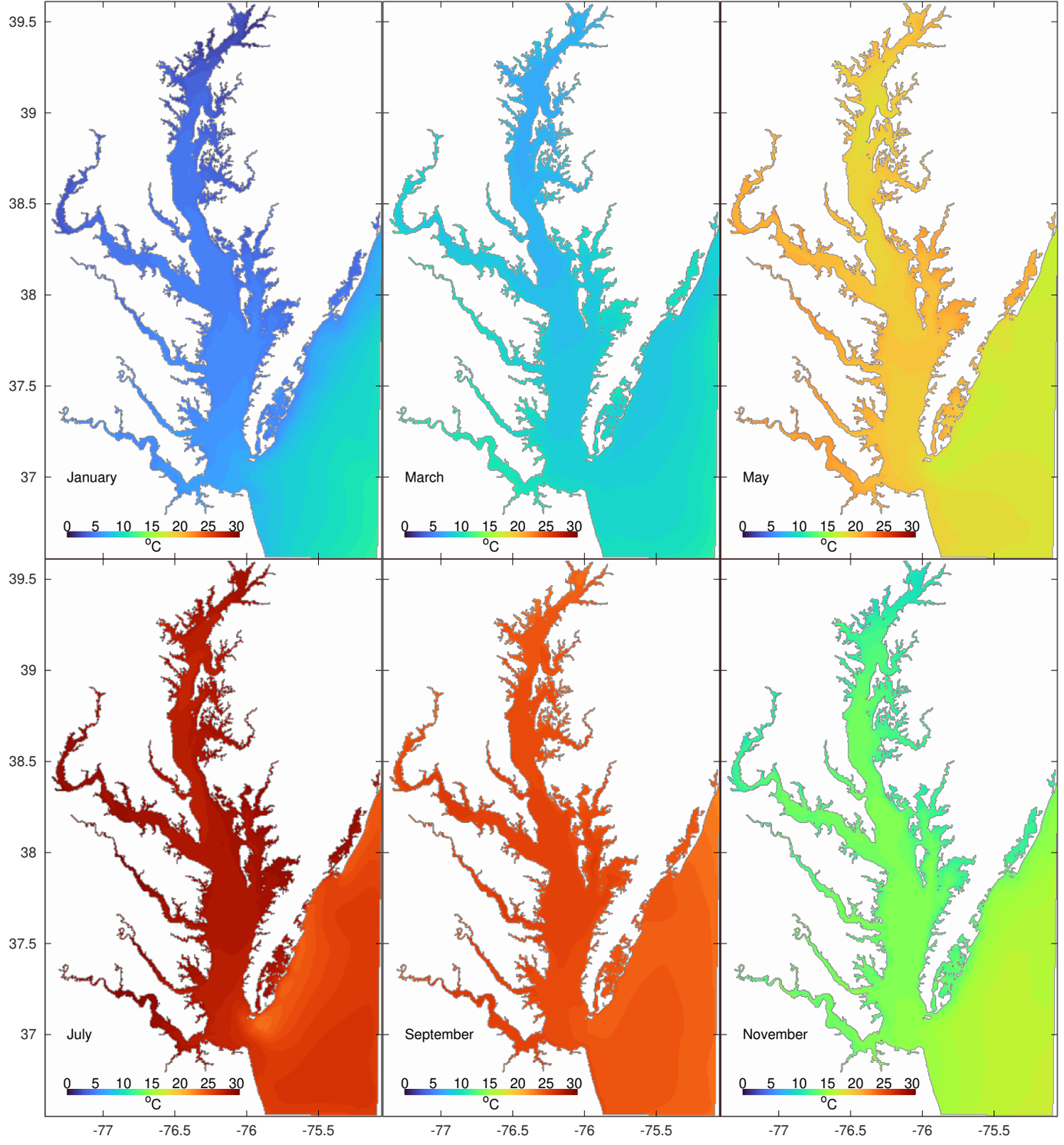

Figure 9: Potential temperature at the surface.

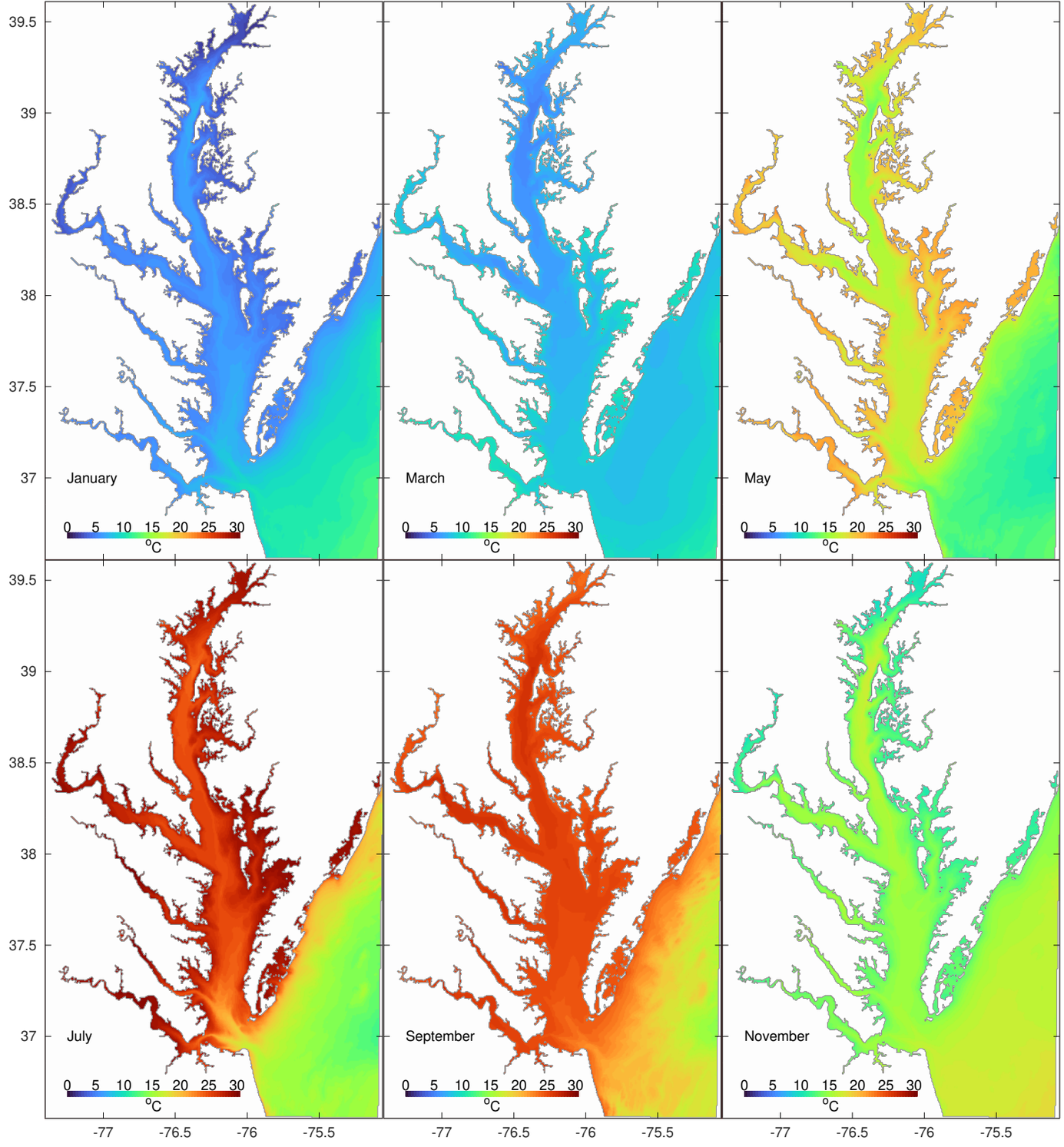

Figure 10: Potential temperature at the bottom.

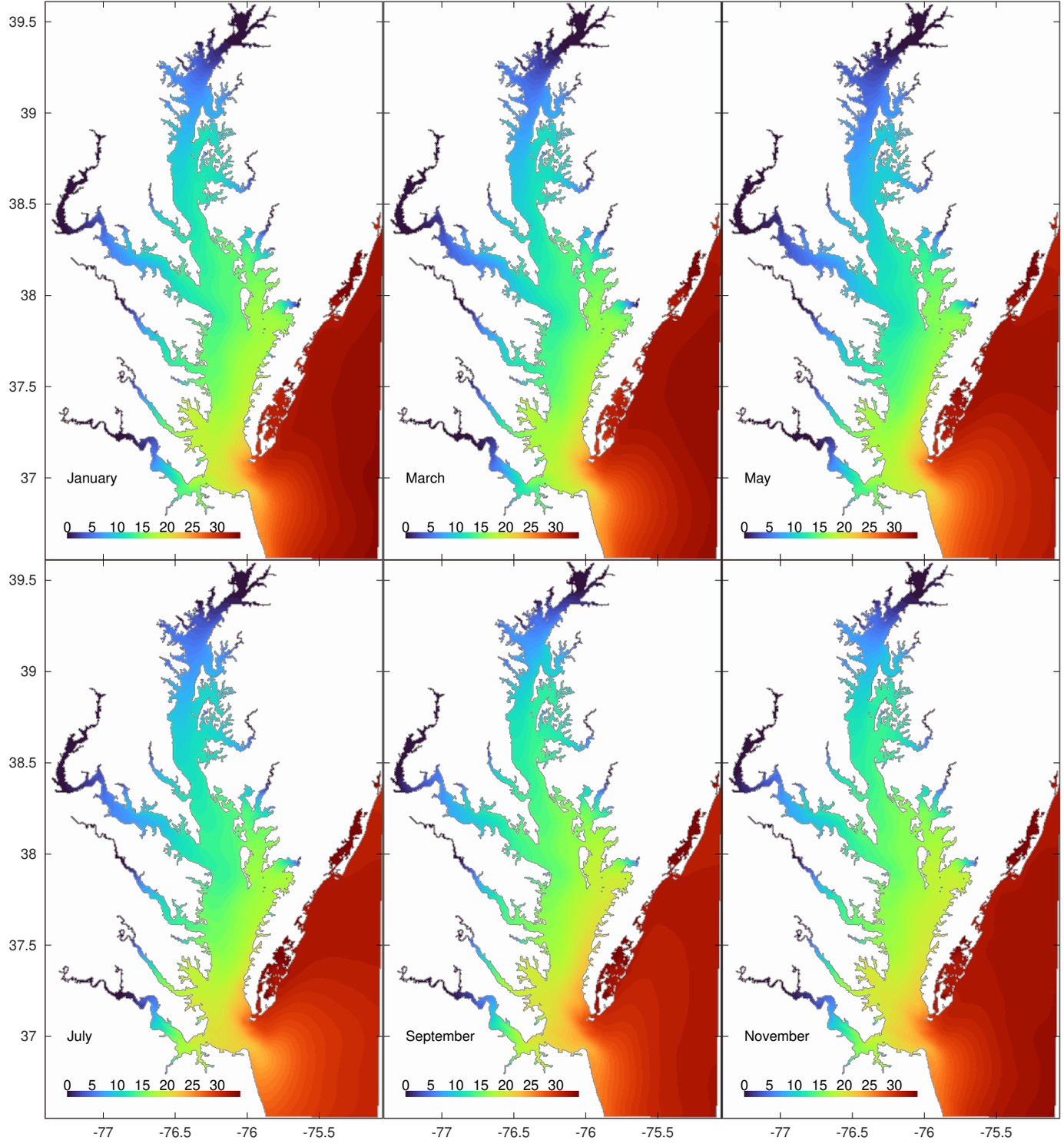

Figure 11: Practical salinity at the surface.

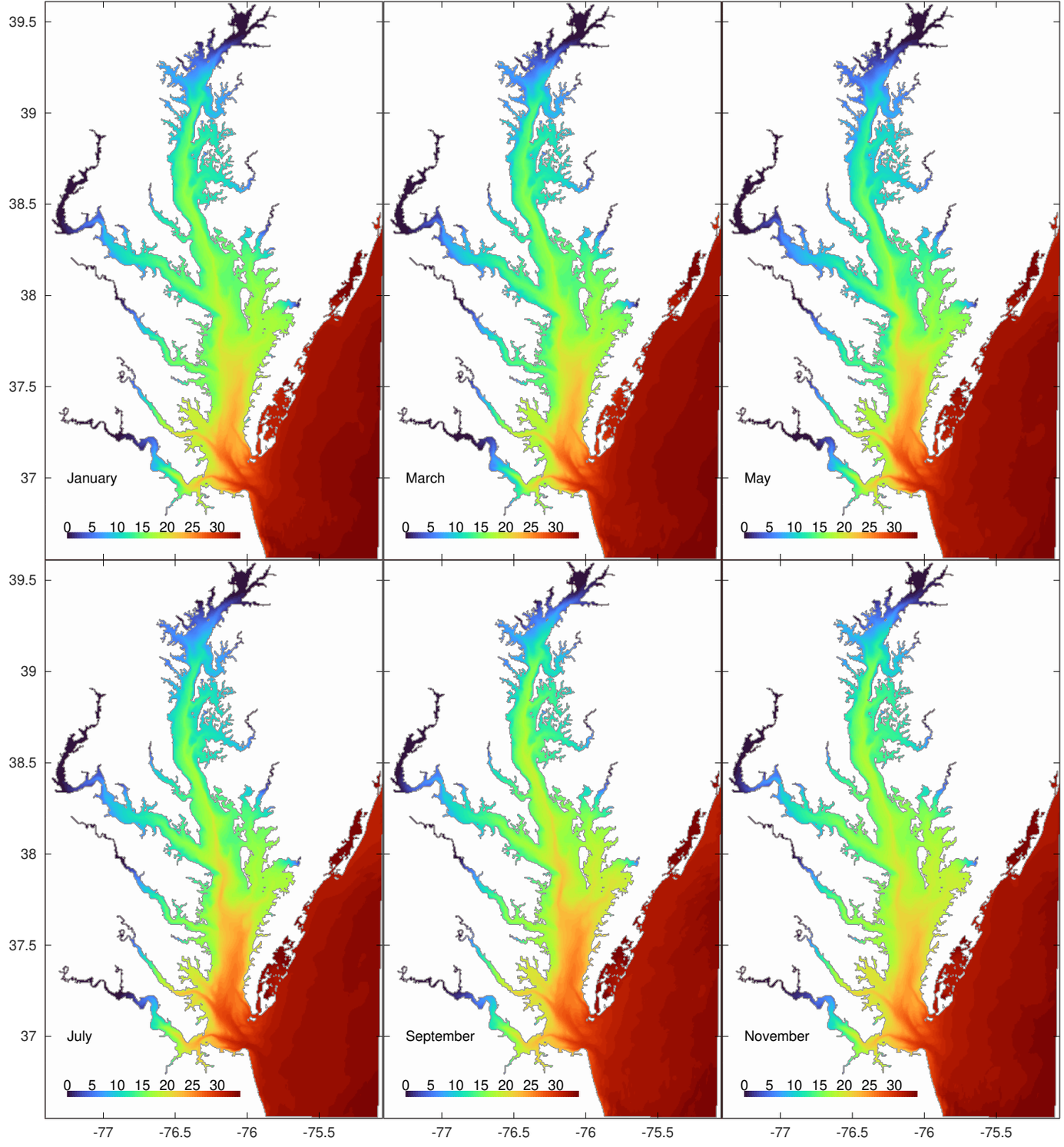

Figure 12: Practical salinity at the bottom.

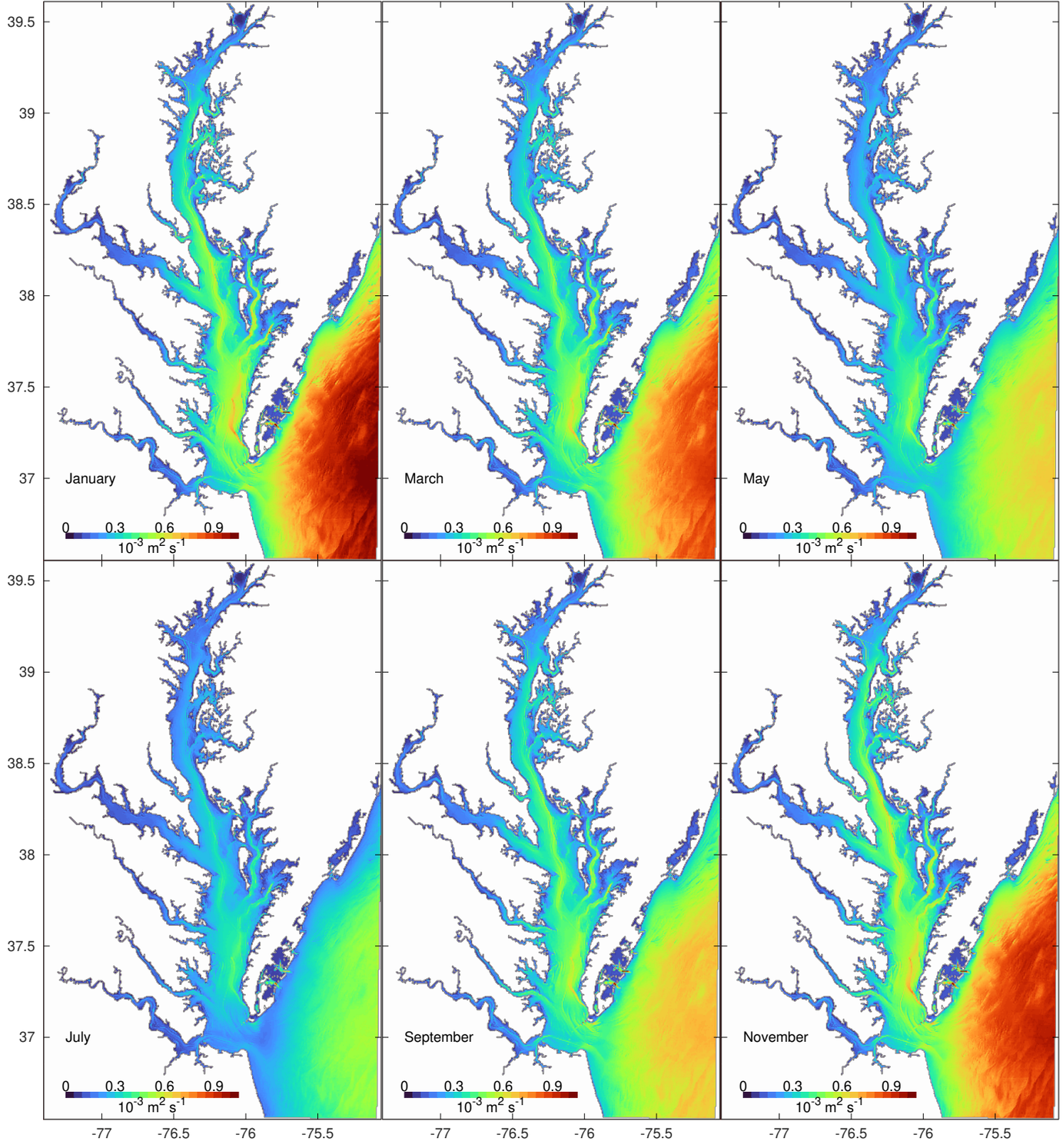

Figure 13: Sub-grid scale vertical diffusivity near the surface.

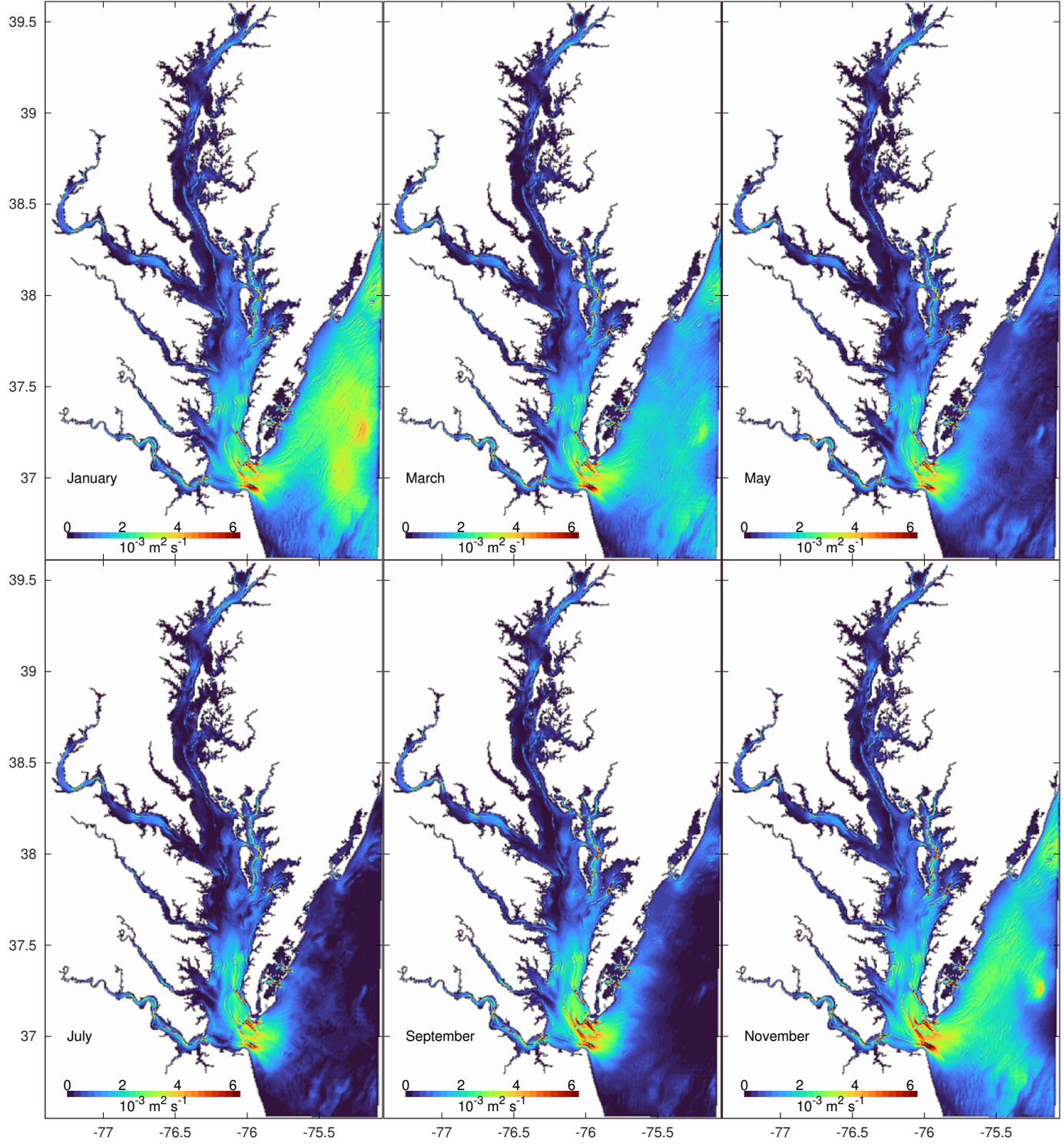

Figure 14: Sub-grid scale vertical diffusivity near the bottom.

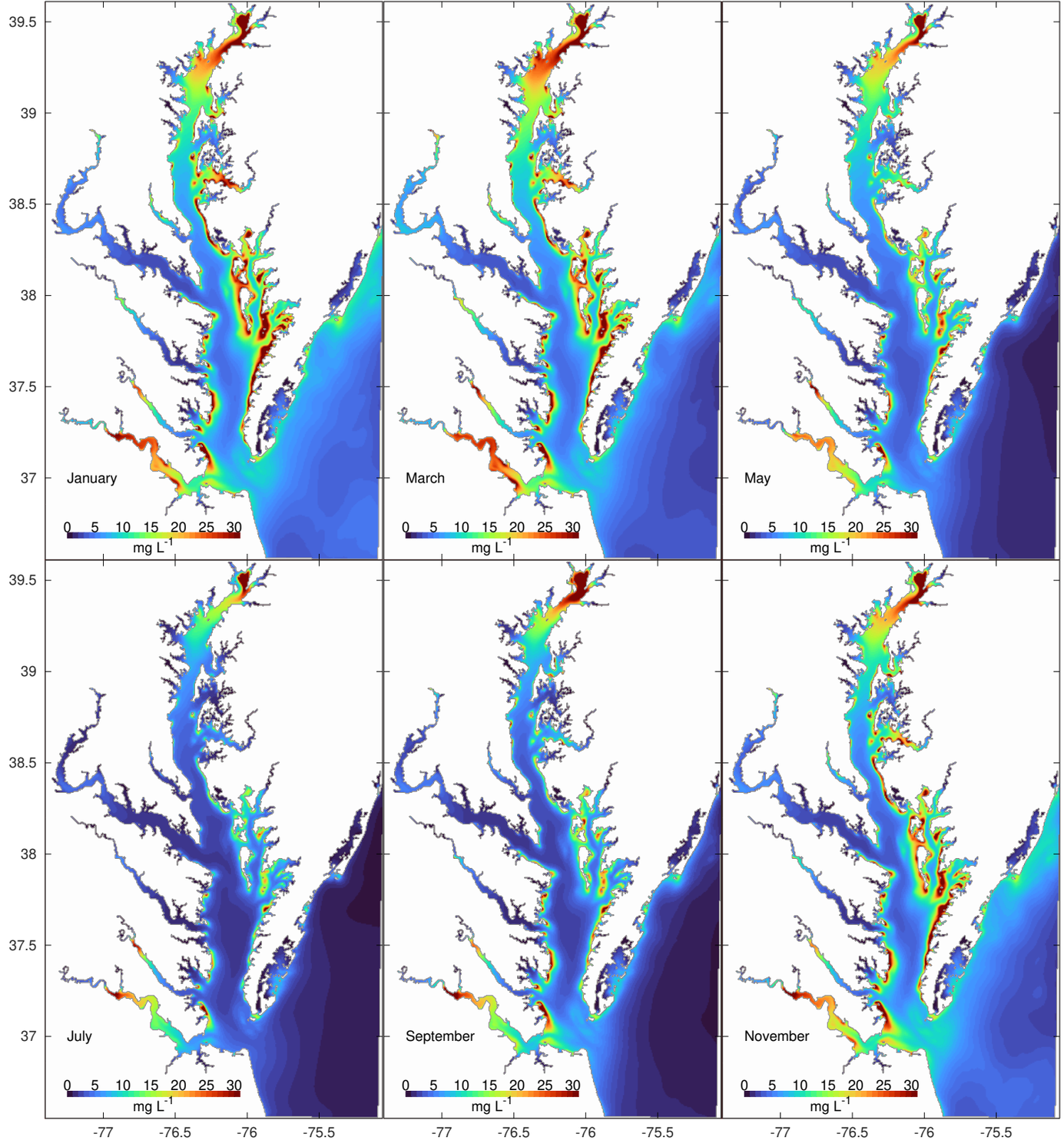

Figure 15: Inorganic suspended solids (ISS) at the surface.

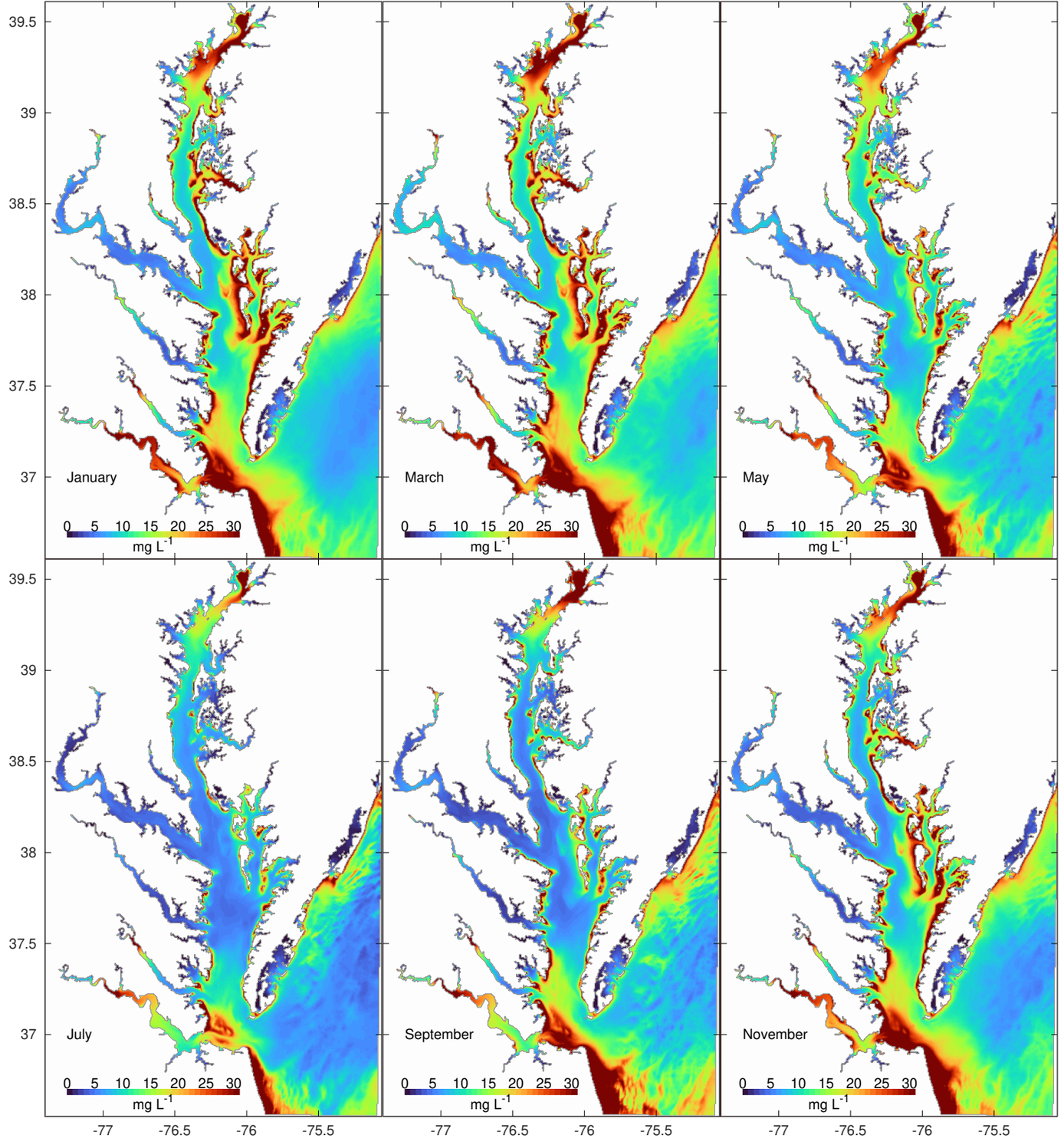

Figure 16: Inorganic suspended solids (ISS) at the bottom.

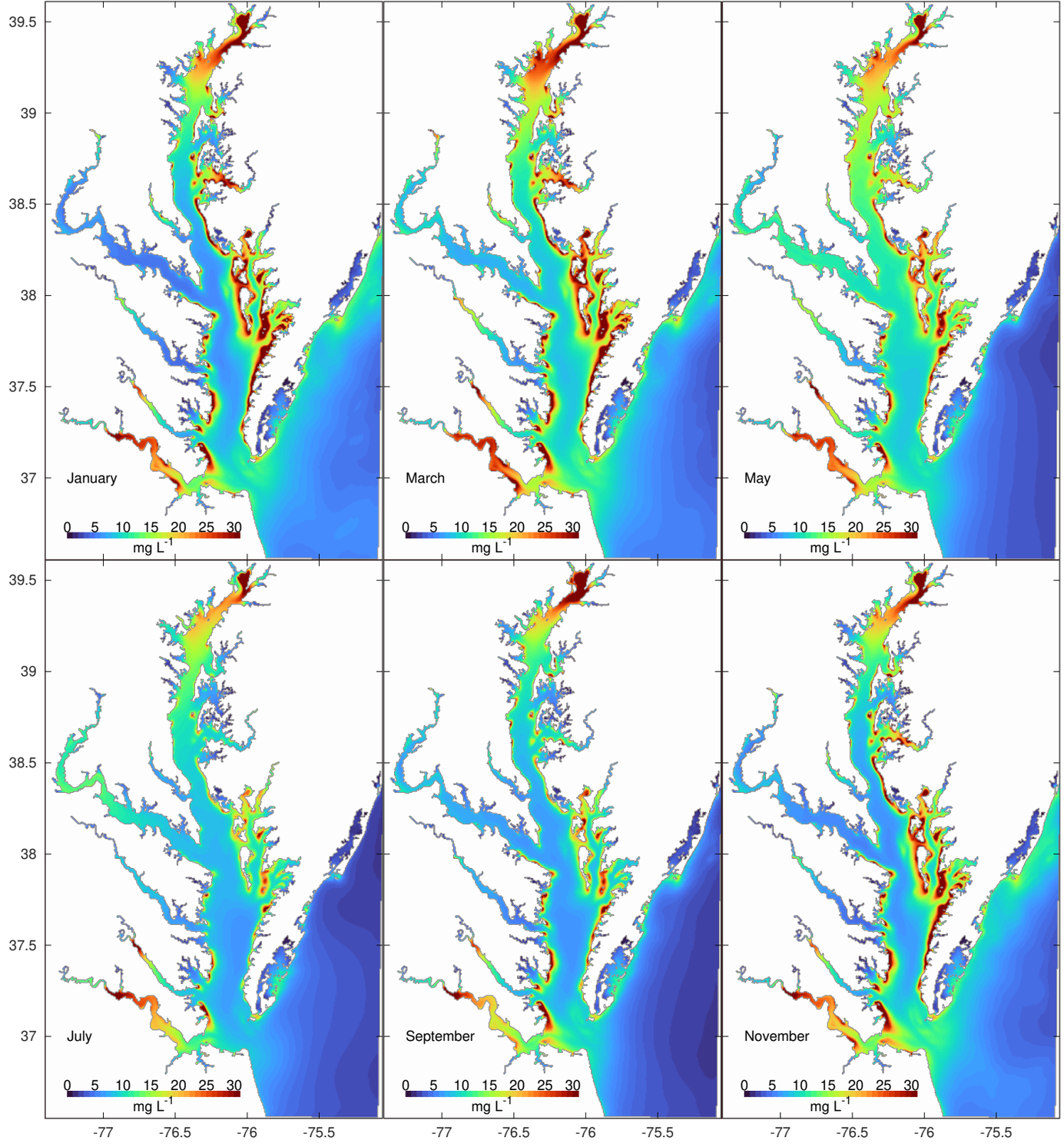

Figure 17: Total suspended solids (TSS) at the surface.

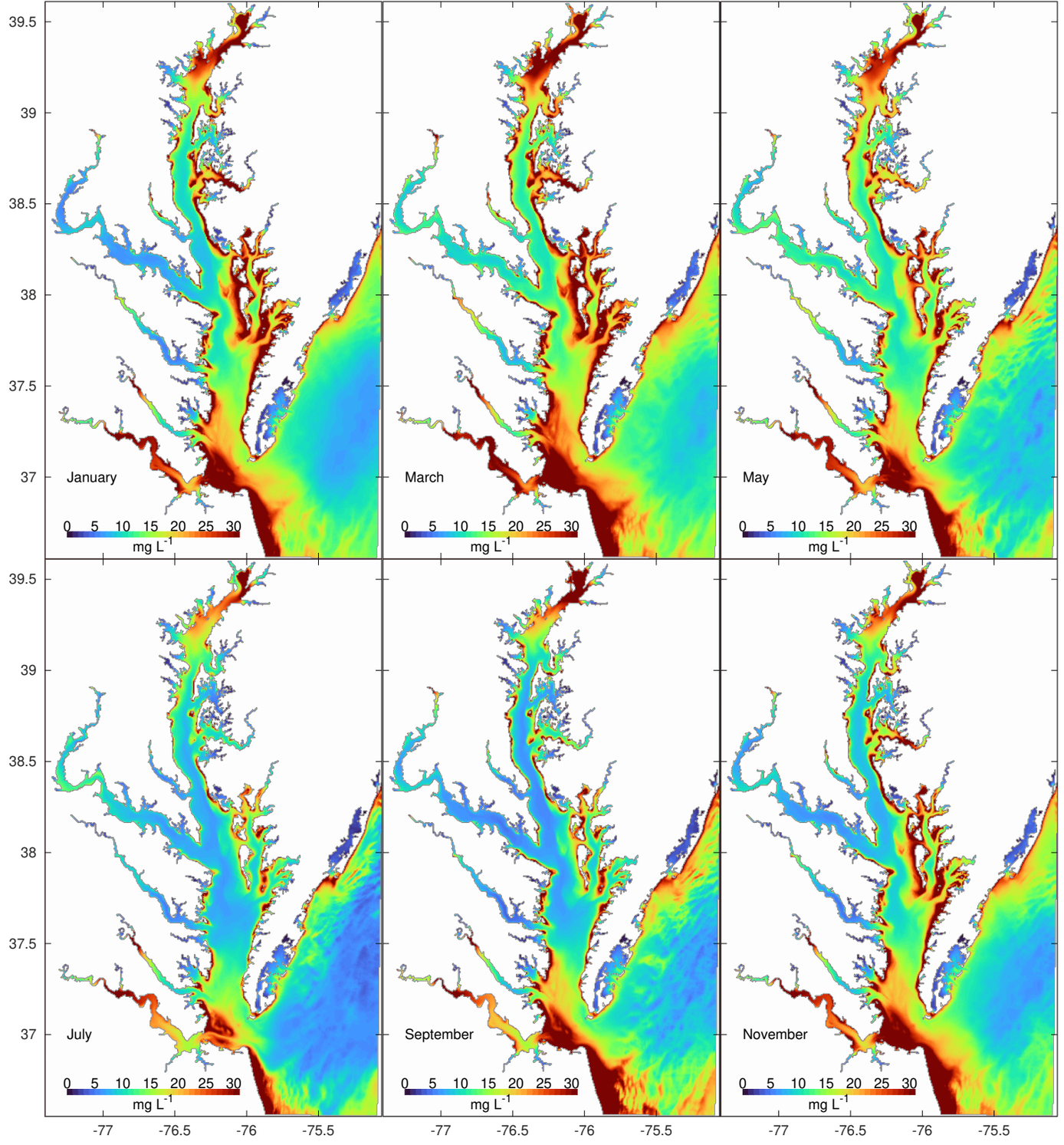

Figure 18: Total suspended solids (TSS) at the bottom.

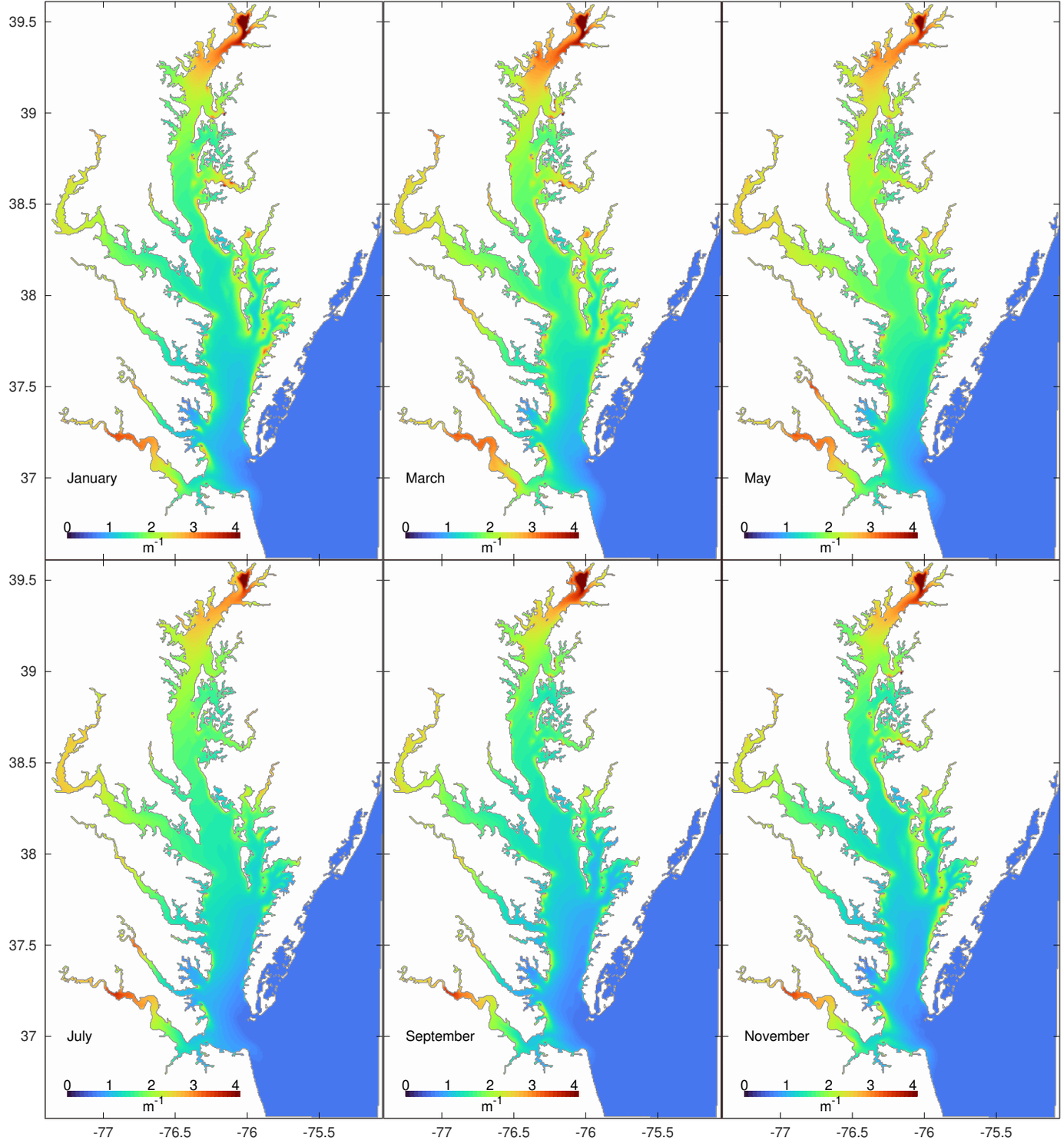

Figure 19: Diffuse light attenuation coefficient (K_d) at the surface.

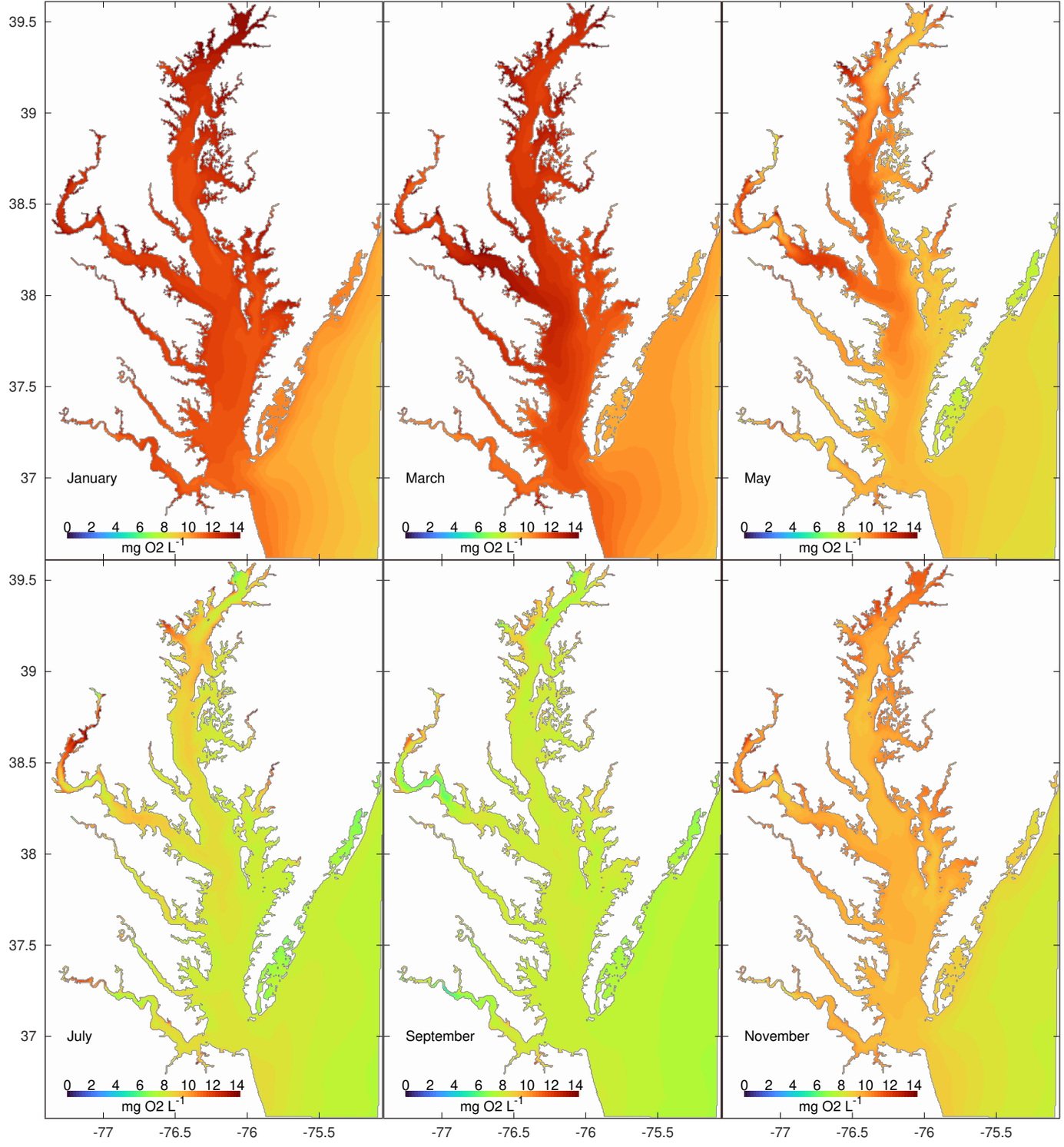

Figure 20: Dissolved dioxygen (O_2) at the surface.

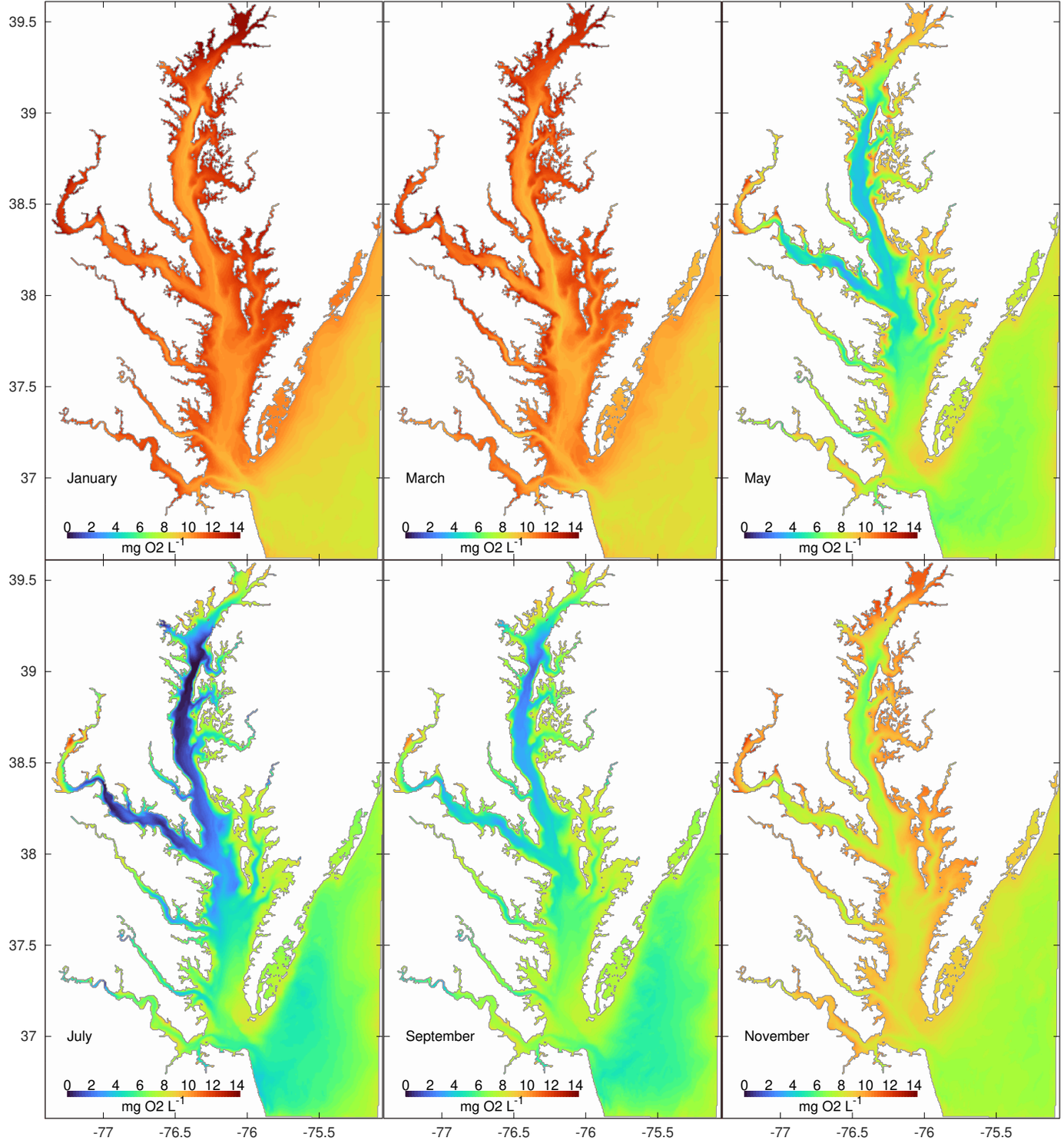

Figure 21: Dissolved dioxygen (O_2) at the bottom.

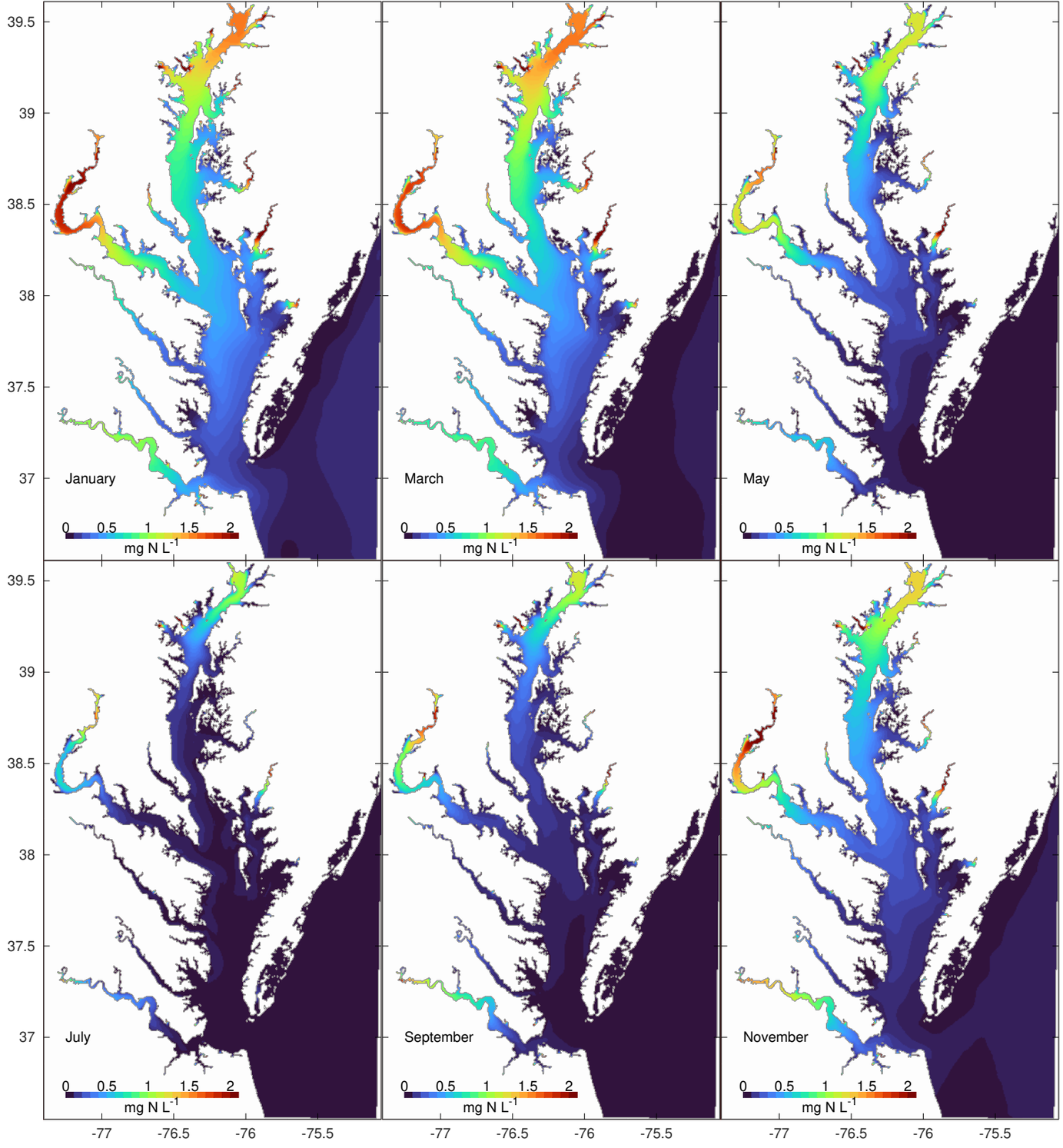

Figure 22: Dissolved inorganic nitrogen (DIN) at the surface.

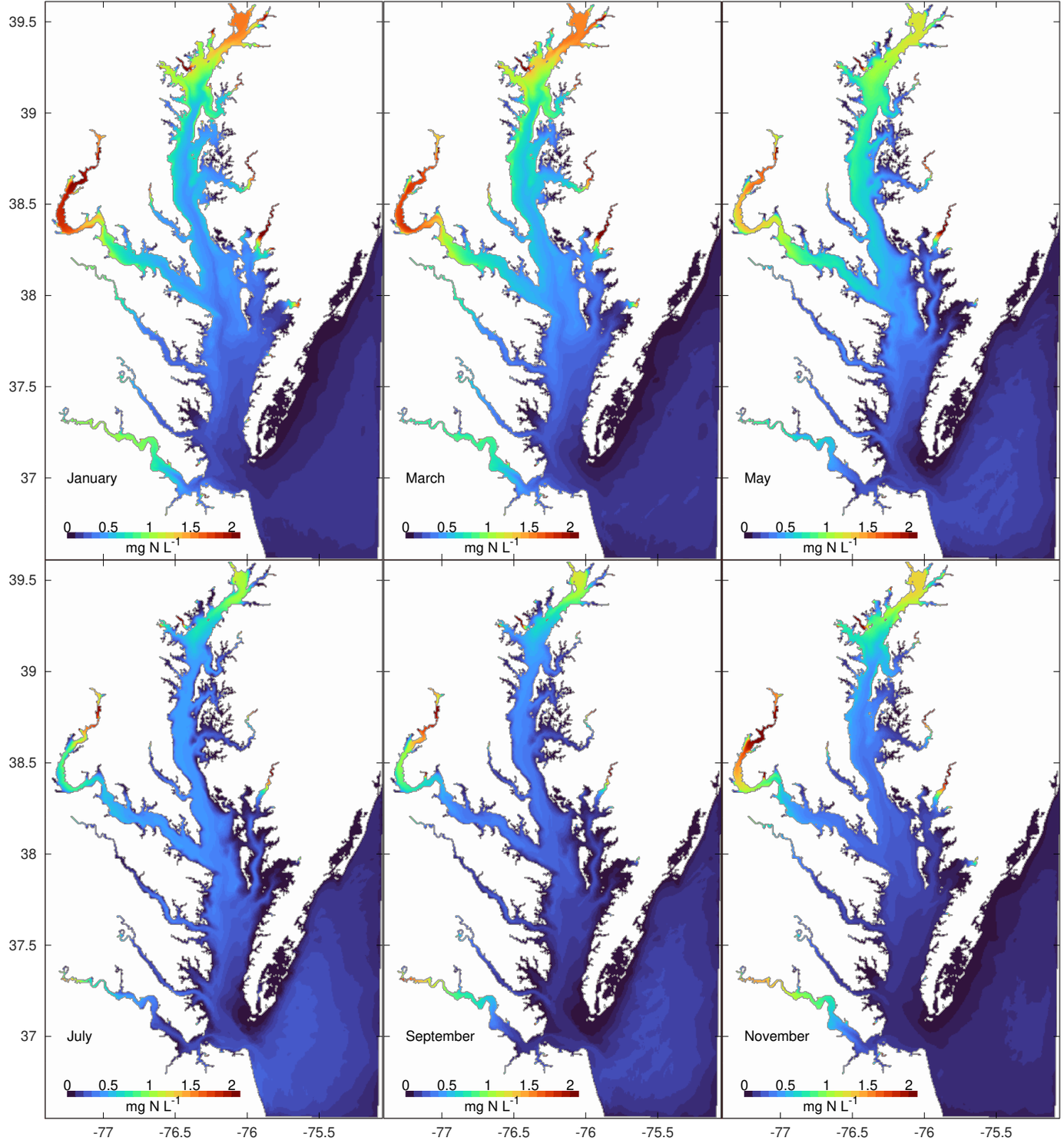

Figure 23: Dissolved inorganic nitrogen (DIN) at the bottom.

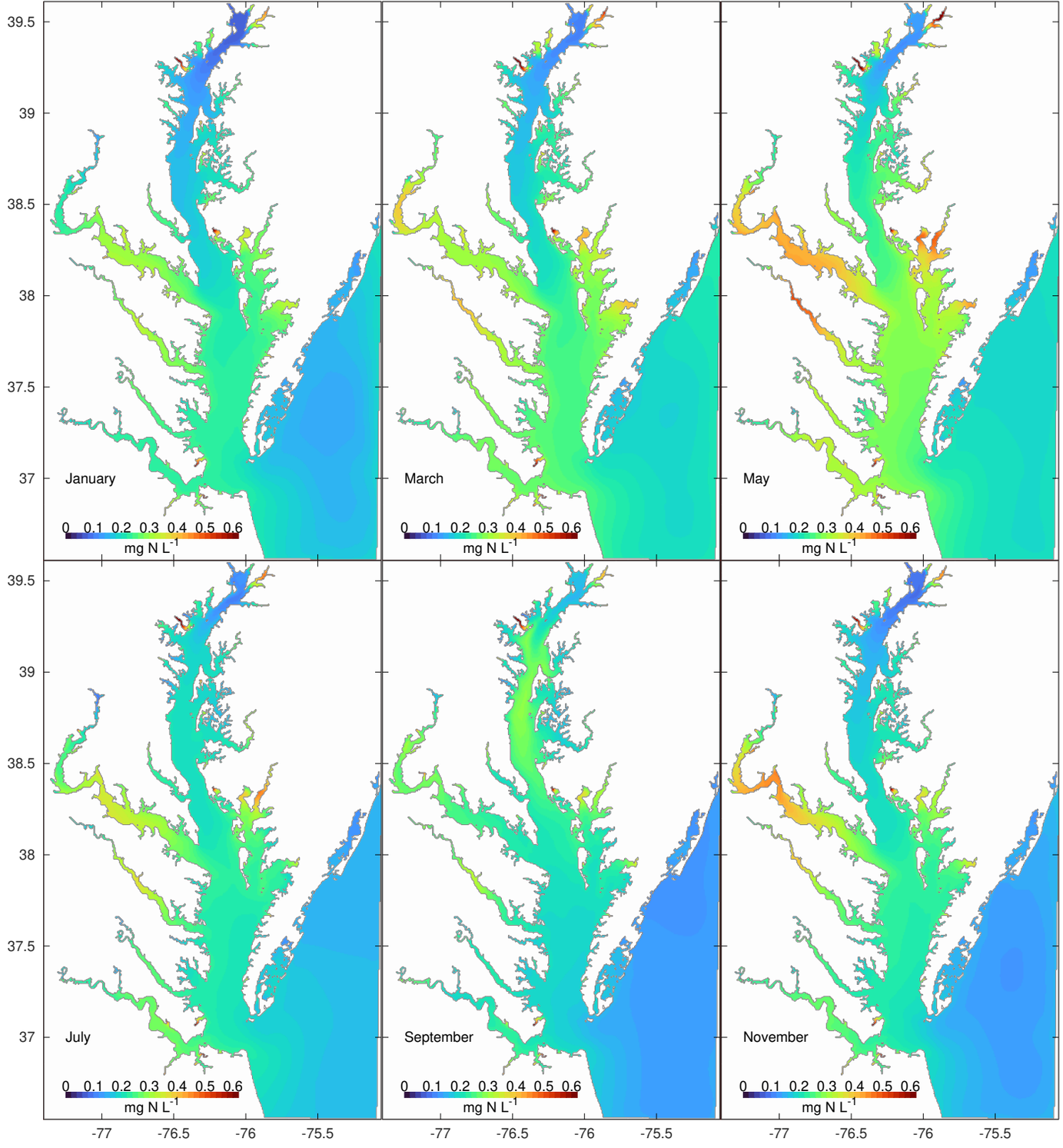

Figure 24: Dissolved organic nitrogen (DON) at the surface.

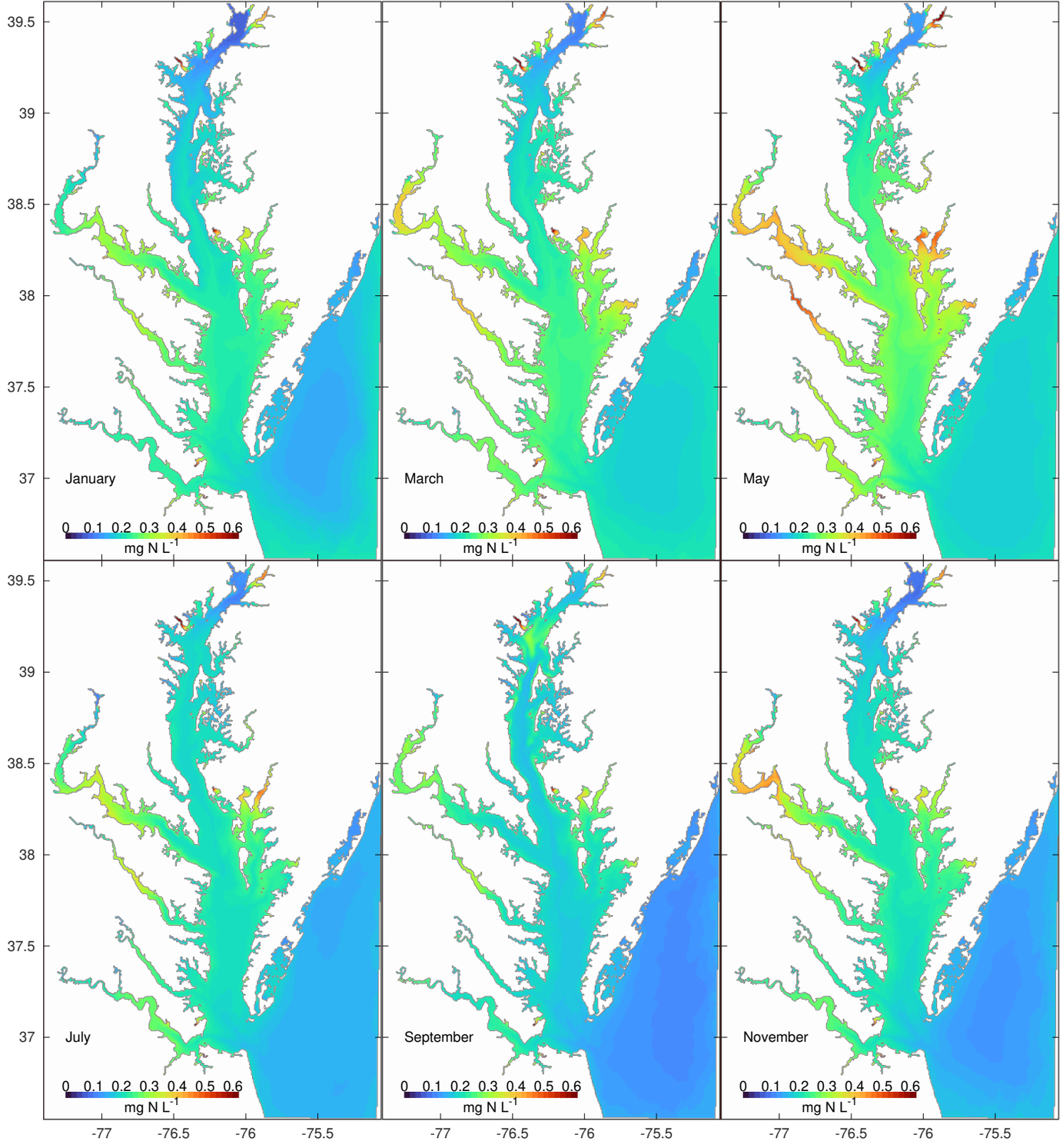

Figure 25: Dissolved organic nitrogen (DON) at the bottom.

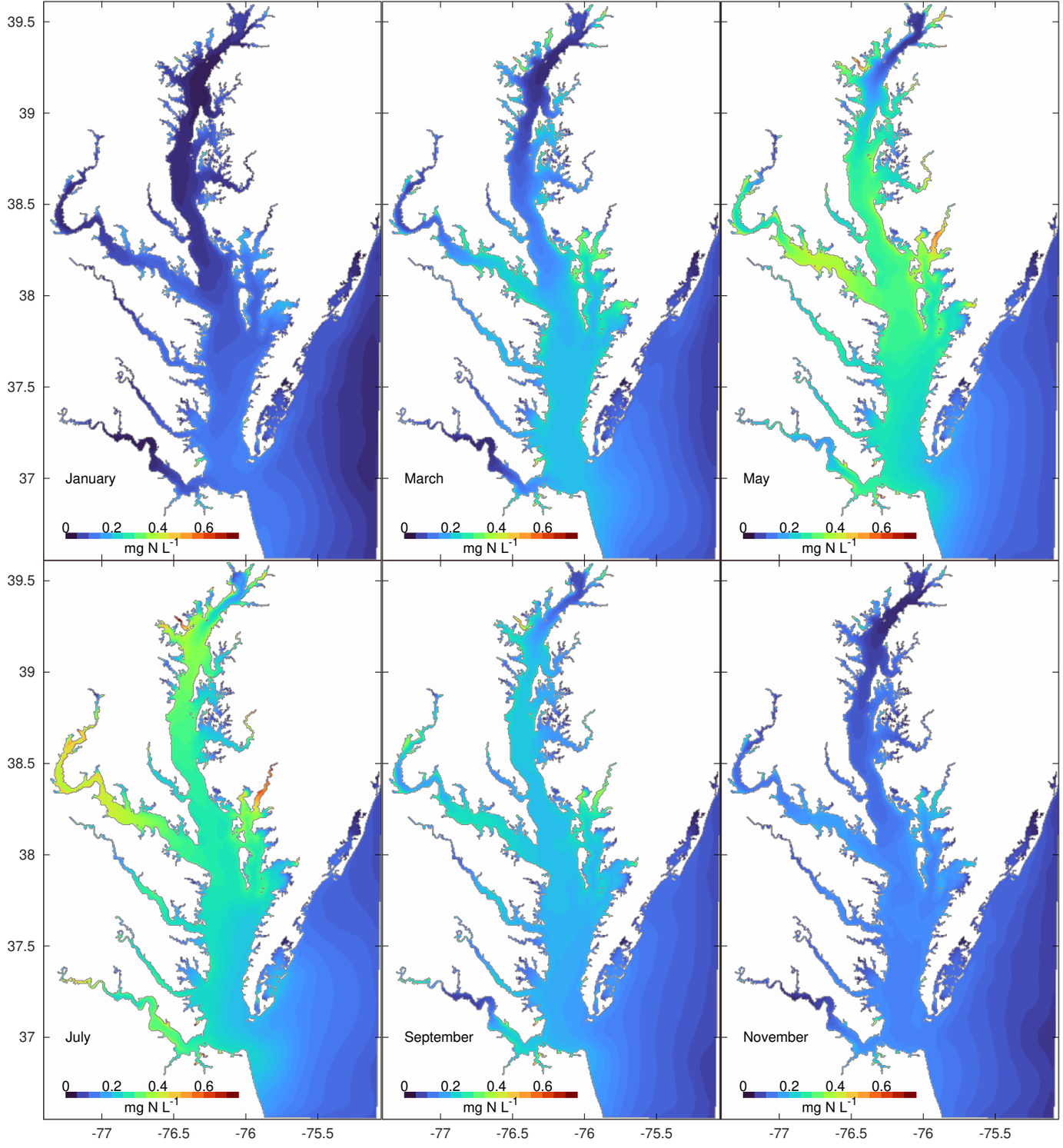

Figure 26: Particulate organic nitrogen (PON) at the surface.

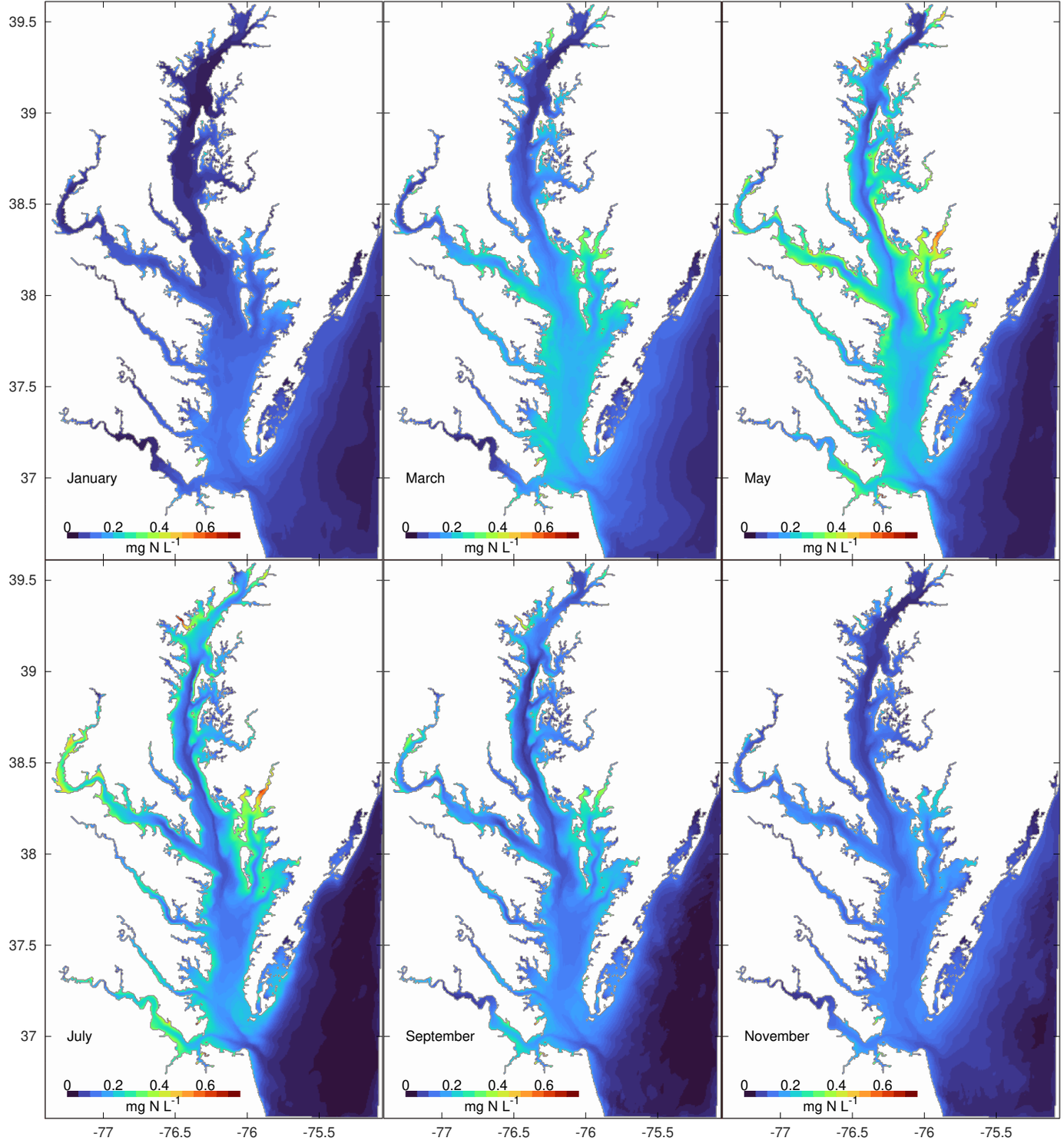

Figure 27: Particulate organic nitrogen (PON) at the bottom.

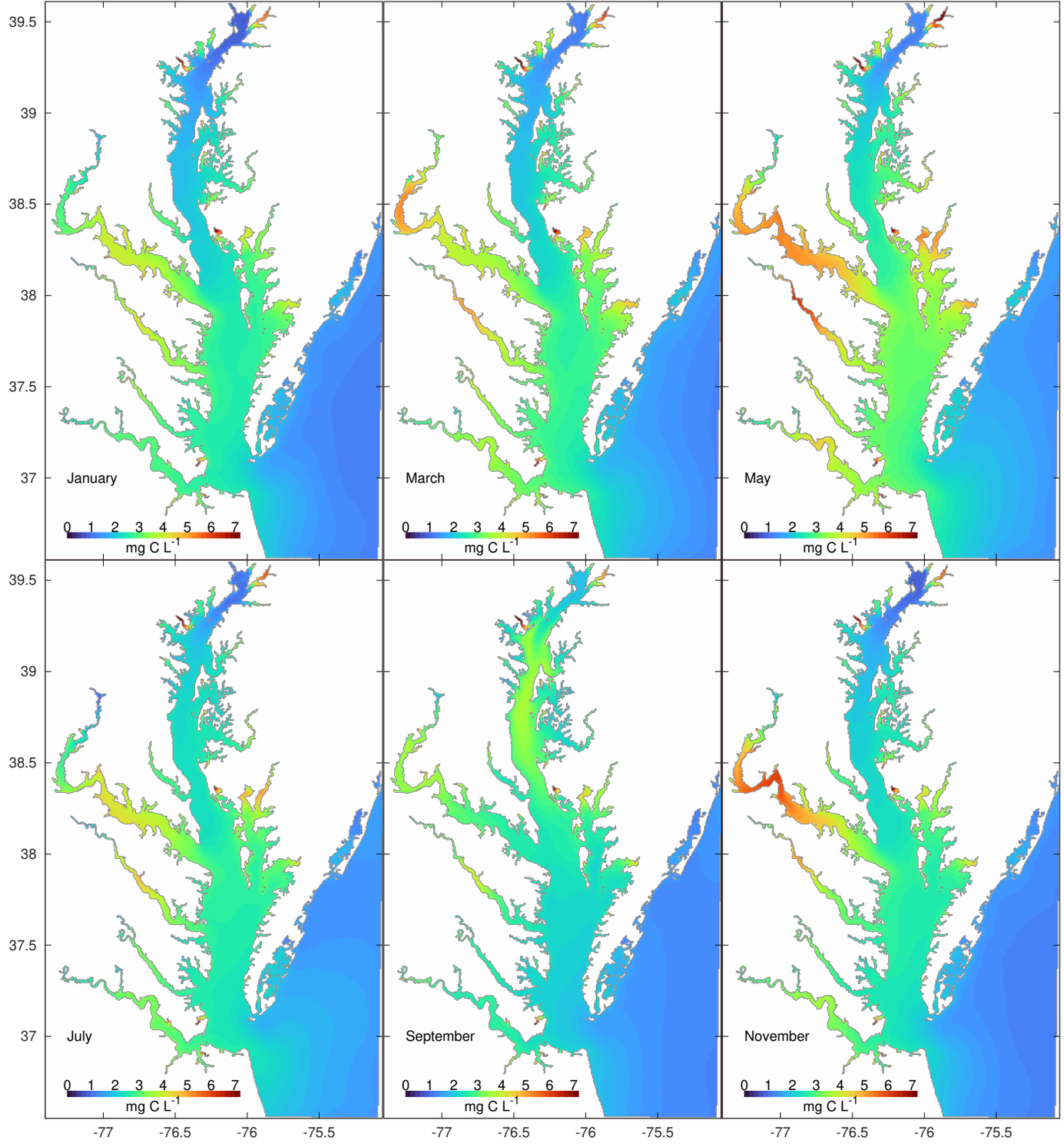

Figure 28: Dissolved organic carbon (DOC) at the surface.

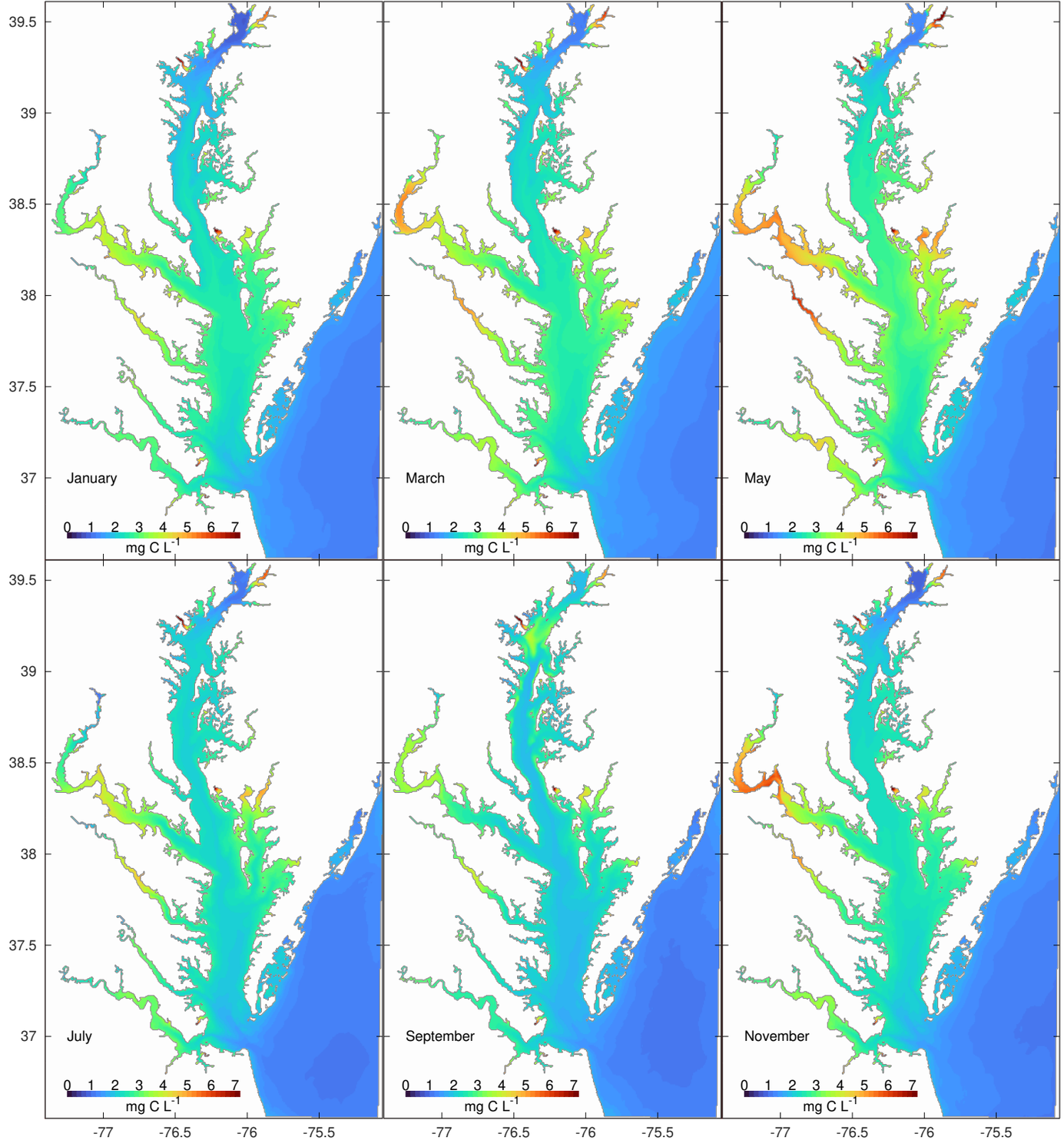

Figure 29: Dissolved organic carbon (DOC) at the bottom.

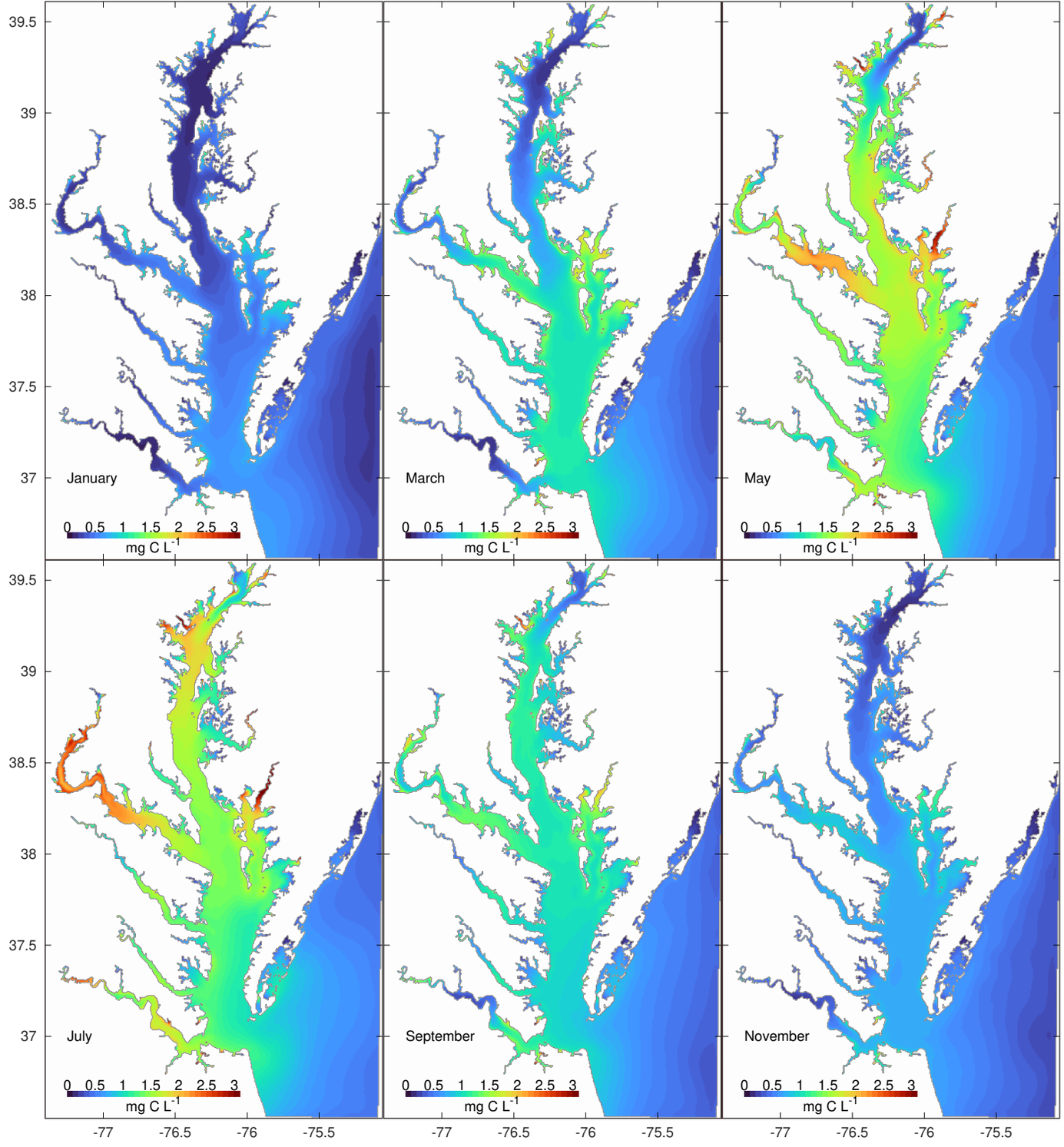

Figure 30: Particulate organic carbon (POC) at the surface.

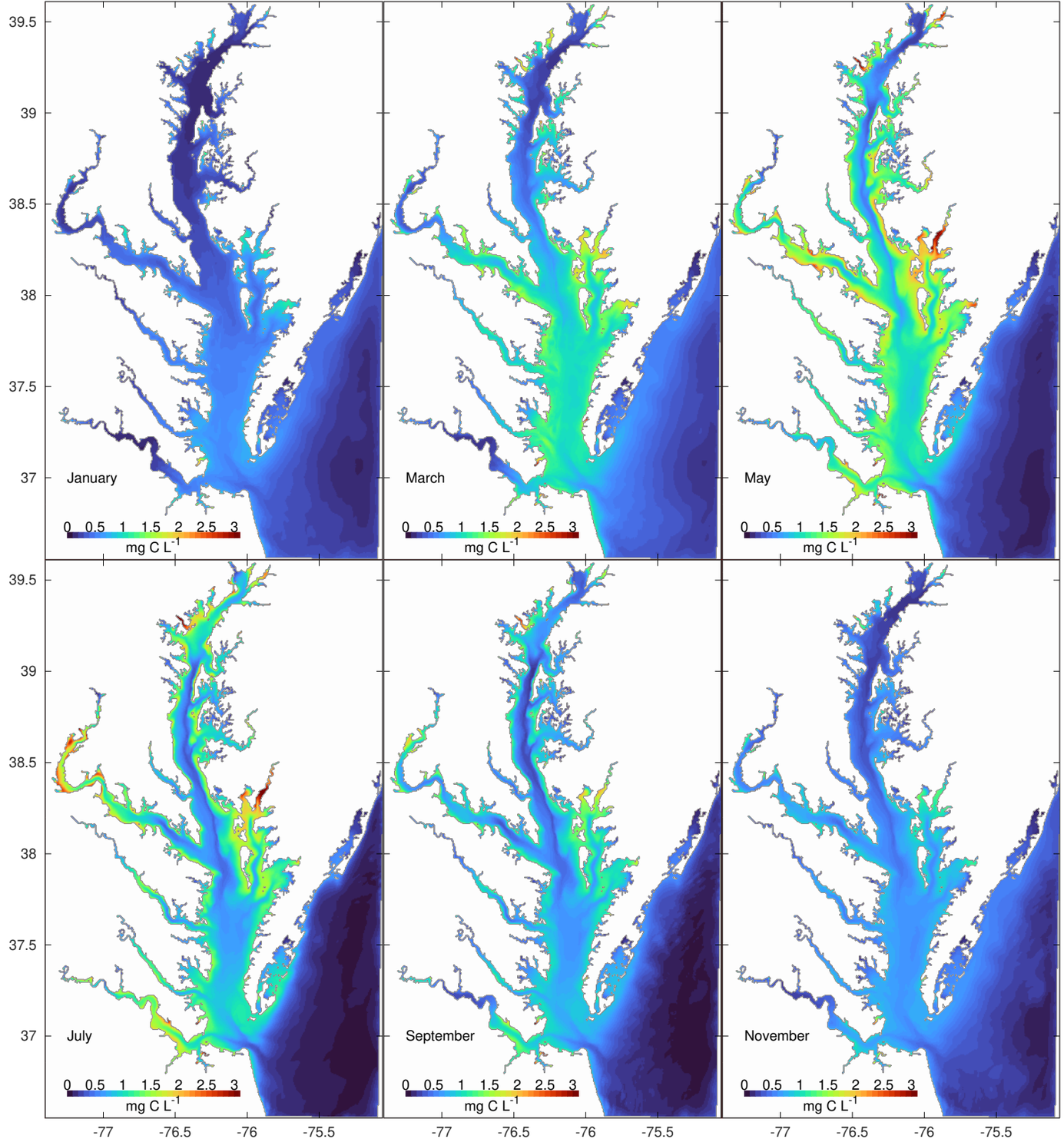

Figure 31: Particulate organic carbon (POC) at the bottom.

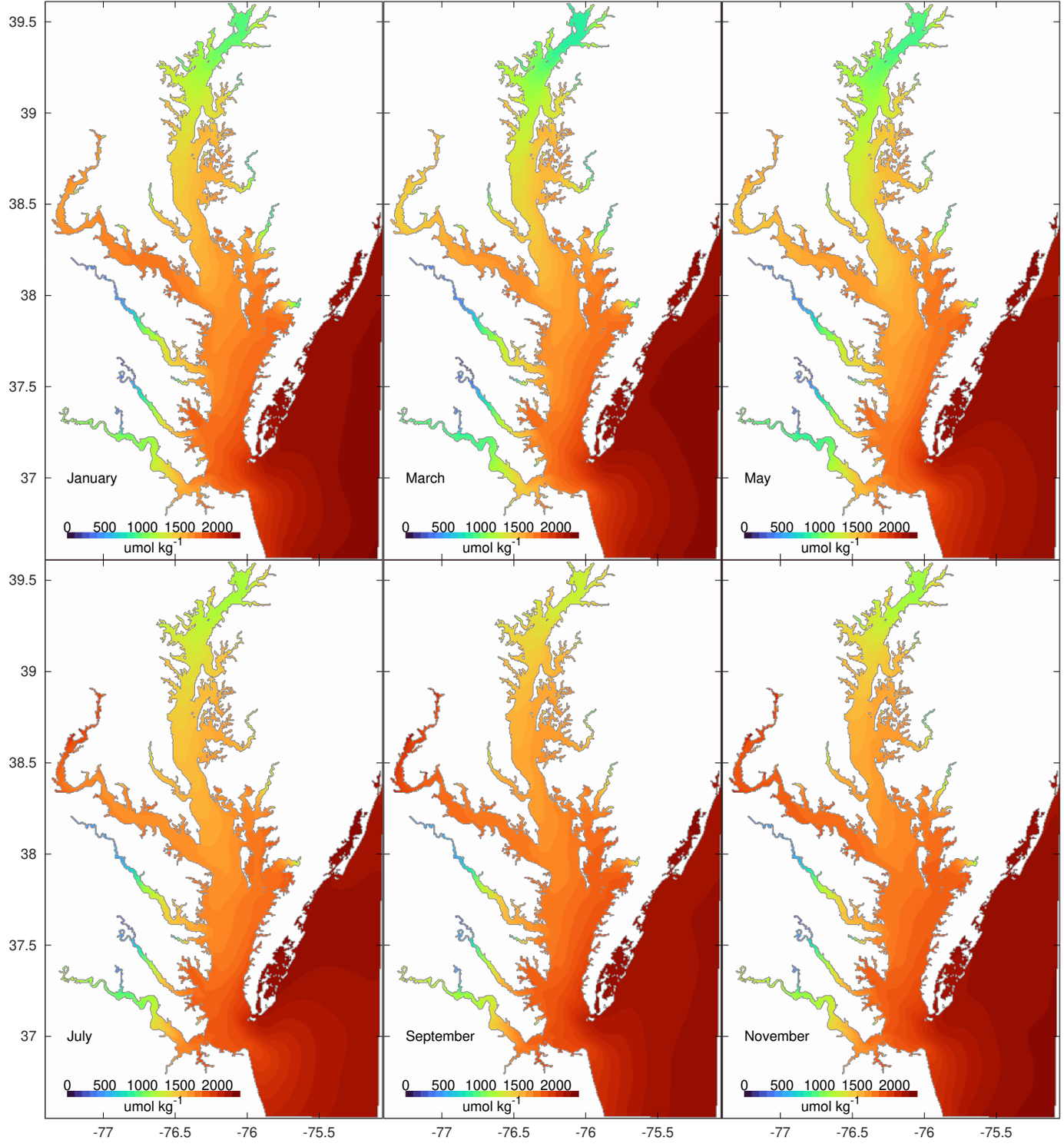

Figure 32: Total alkalinity (TA) at the surface.

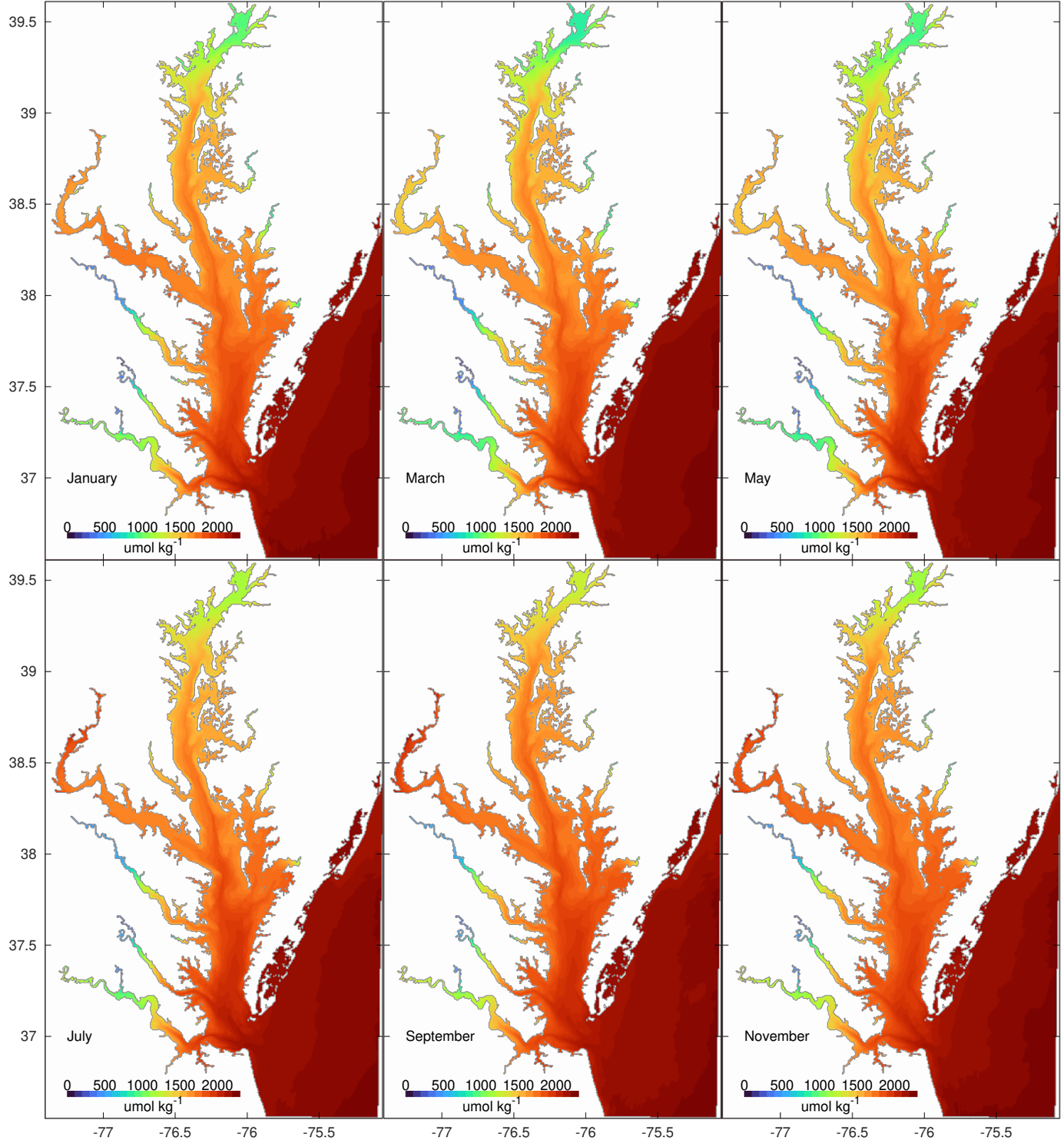

Figure 33: Total alkalinity (TA) at the bottom.

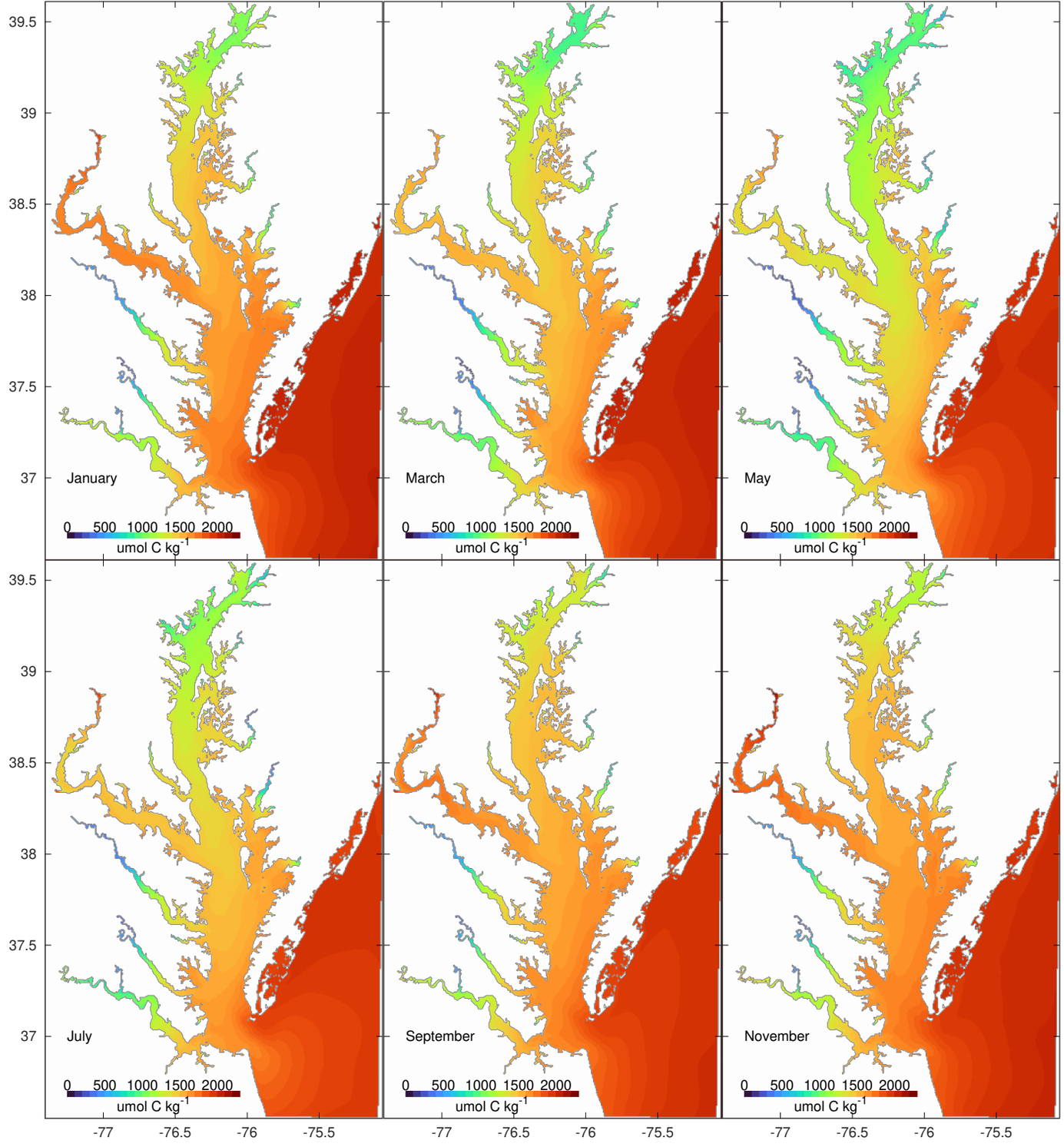

Figure 34: Dissolved inorganic carbon (DIC) at the surface.

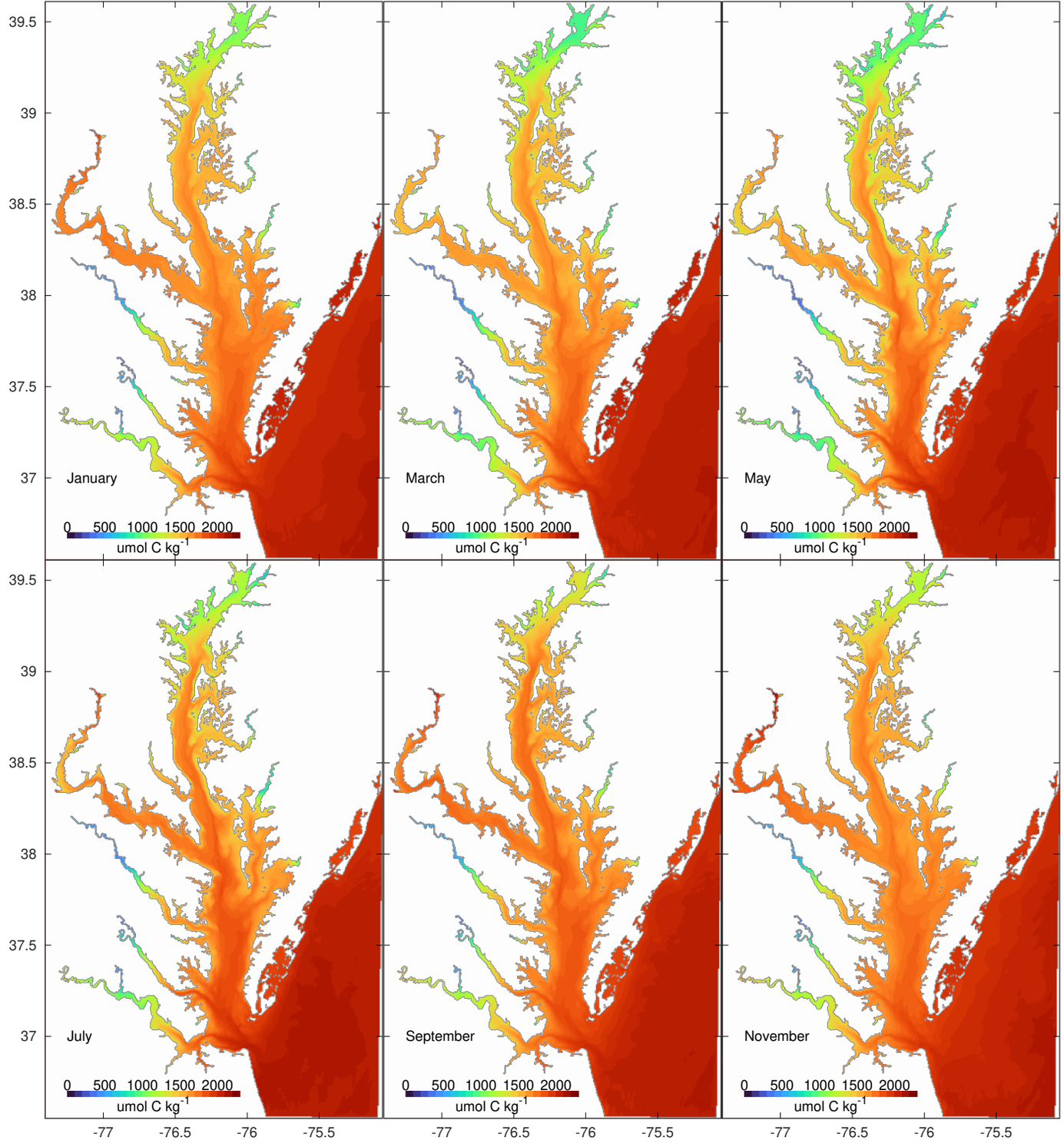

Figure 35: Dissolved inorganic carbon (DIC) at the bottom.

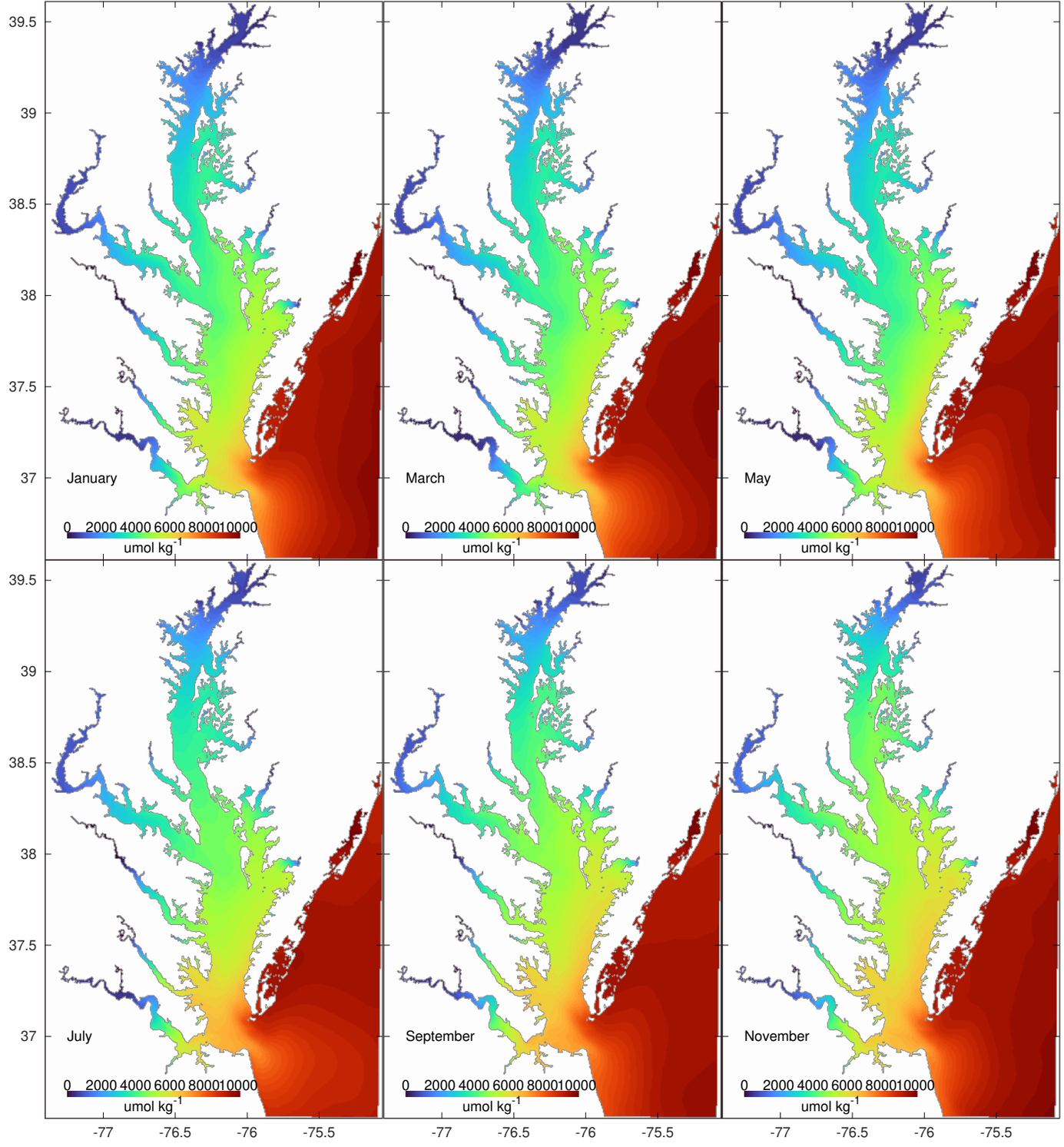

Figure 36: Dissolved calcium at the surface. In the case of this particular variable, the climatology is based on the period 2021–2023.

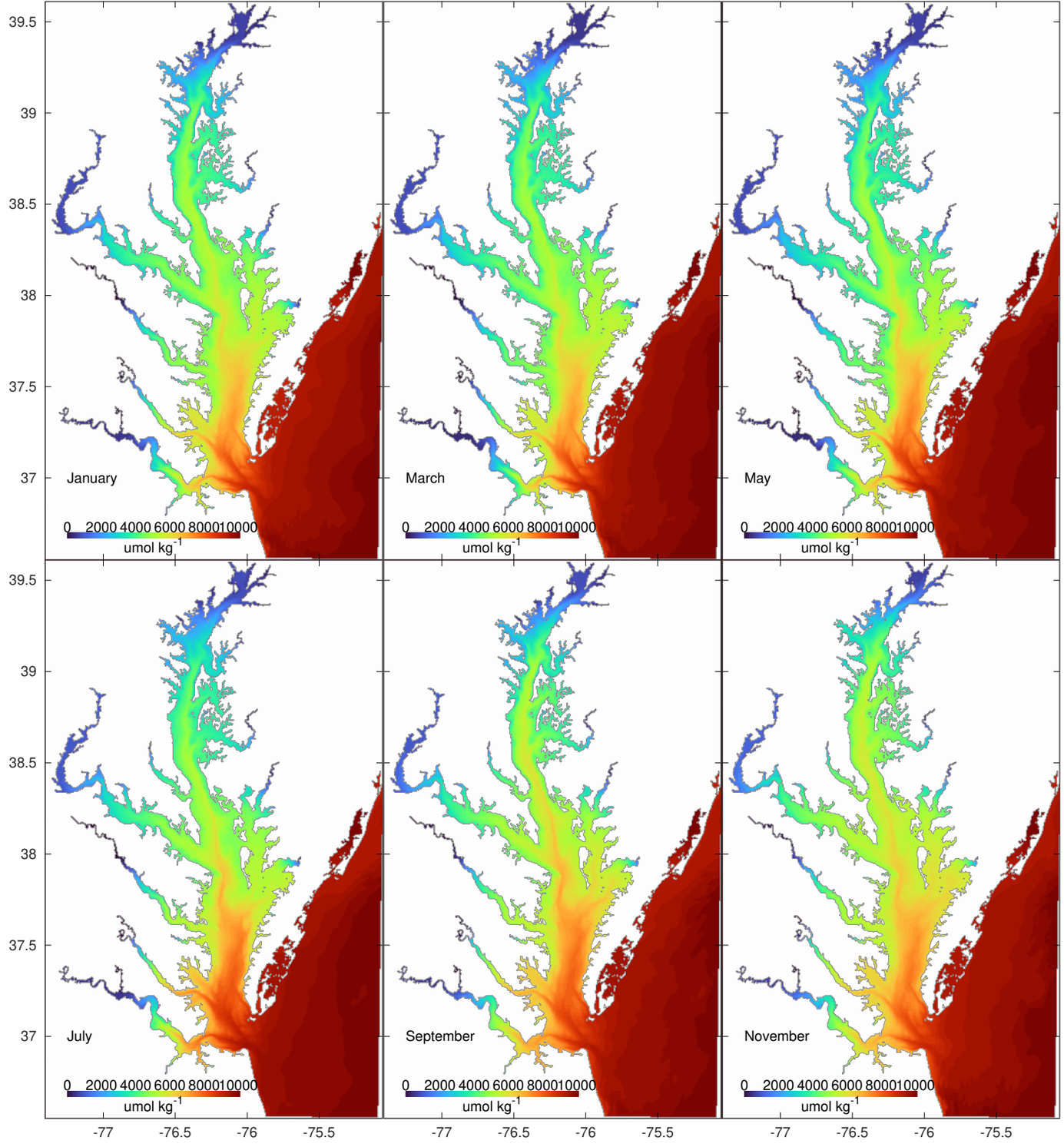

Figure 37: Dissolved calcium at the bottom. In the case of this particular variable, the climatology is based on the period 2021–2023.

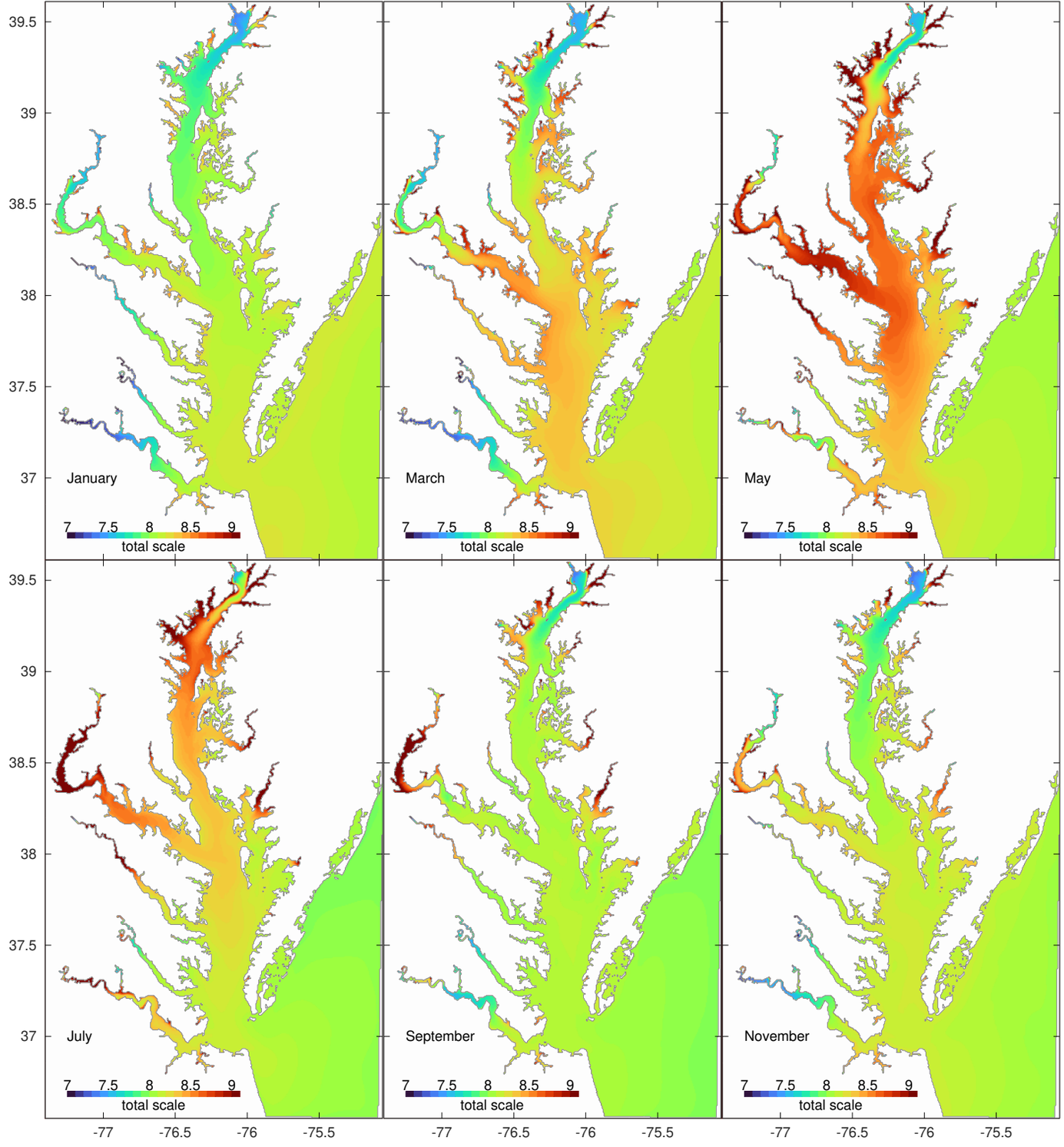

Figure 38: pH at the surface.

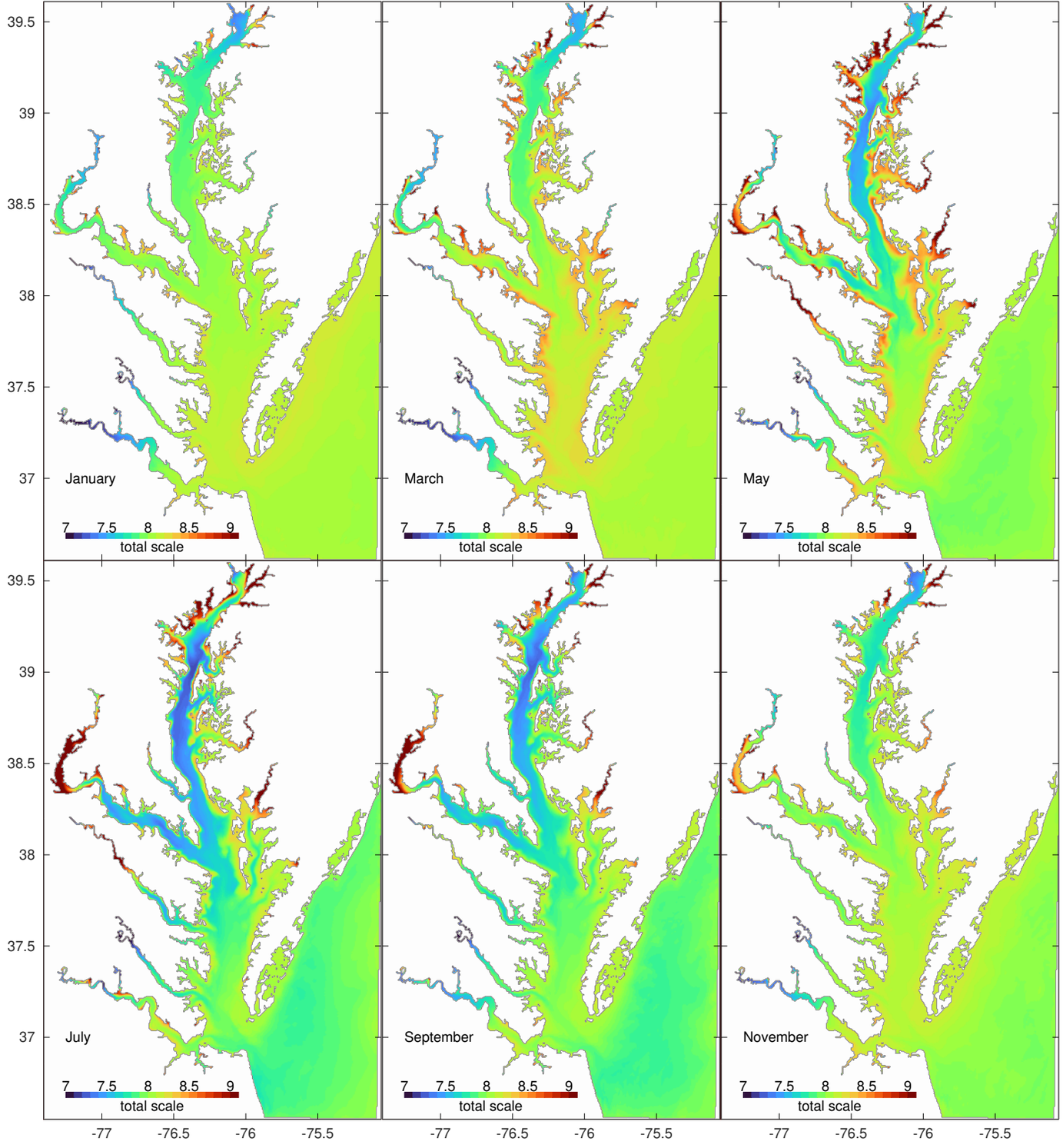

Figure 39: pH at the bottom.

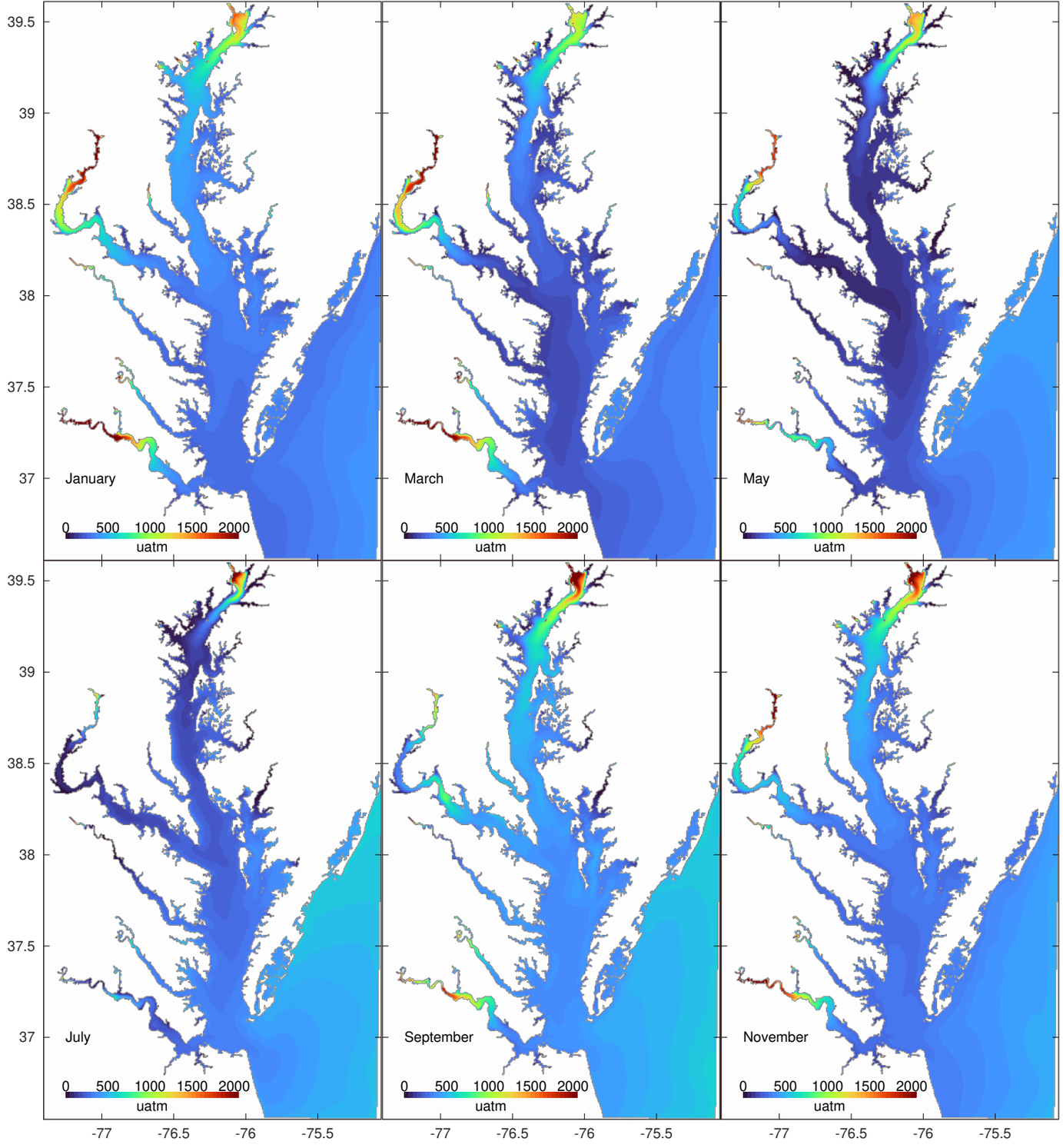

Figure 40: Partial pressure of carbon dioxide (pCO_2) at the surface.

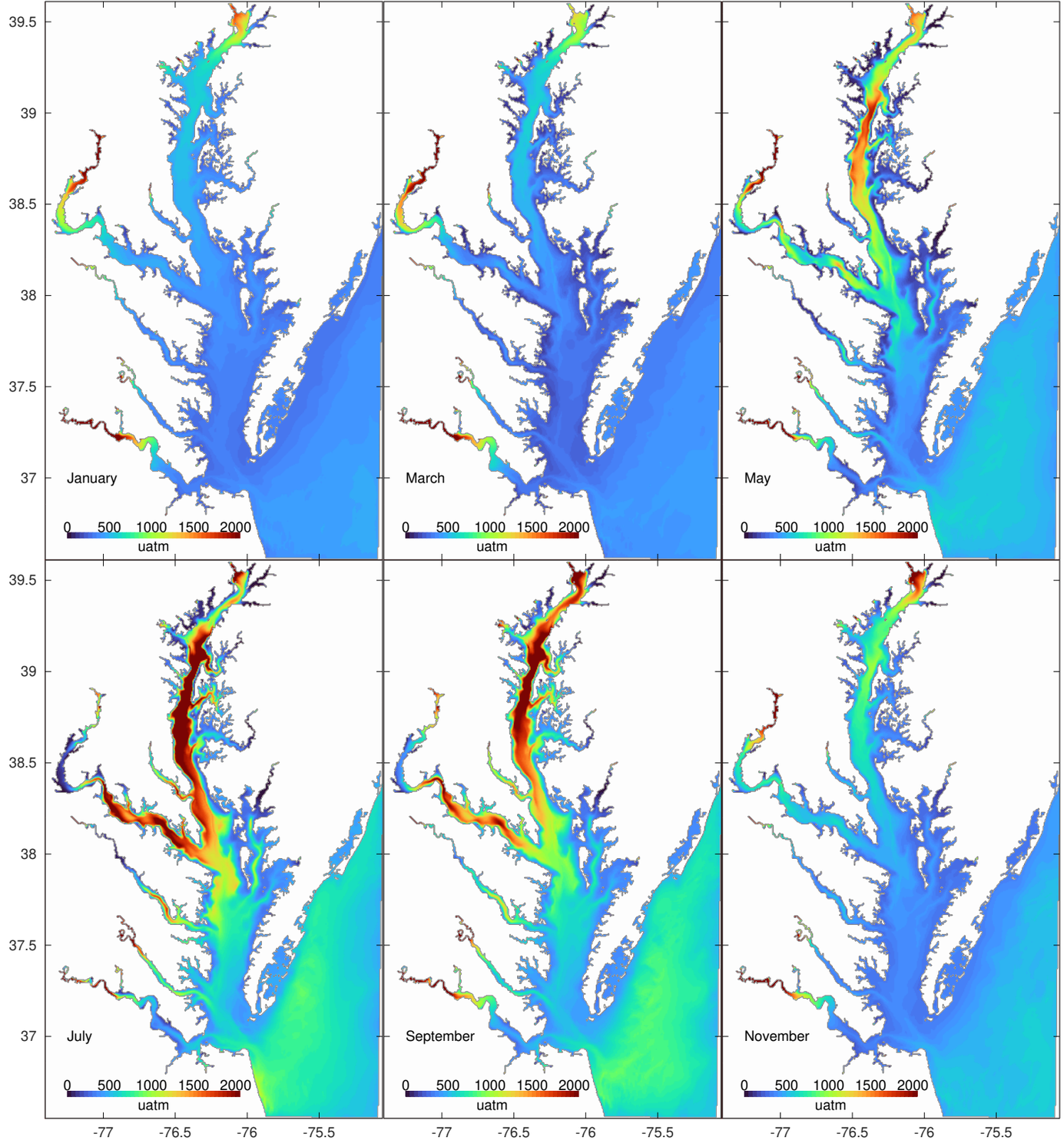

Figure 41: Partial pressure of carbon dioxide (pCO_2) at the bottom.

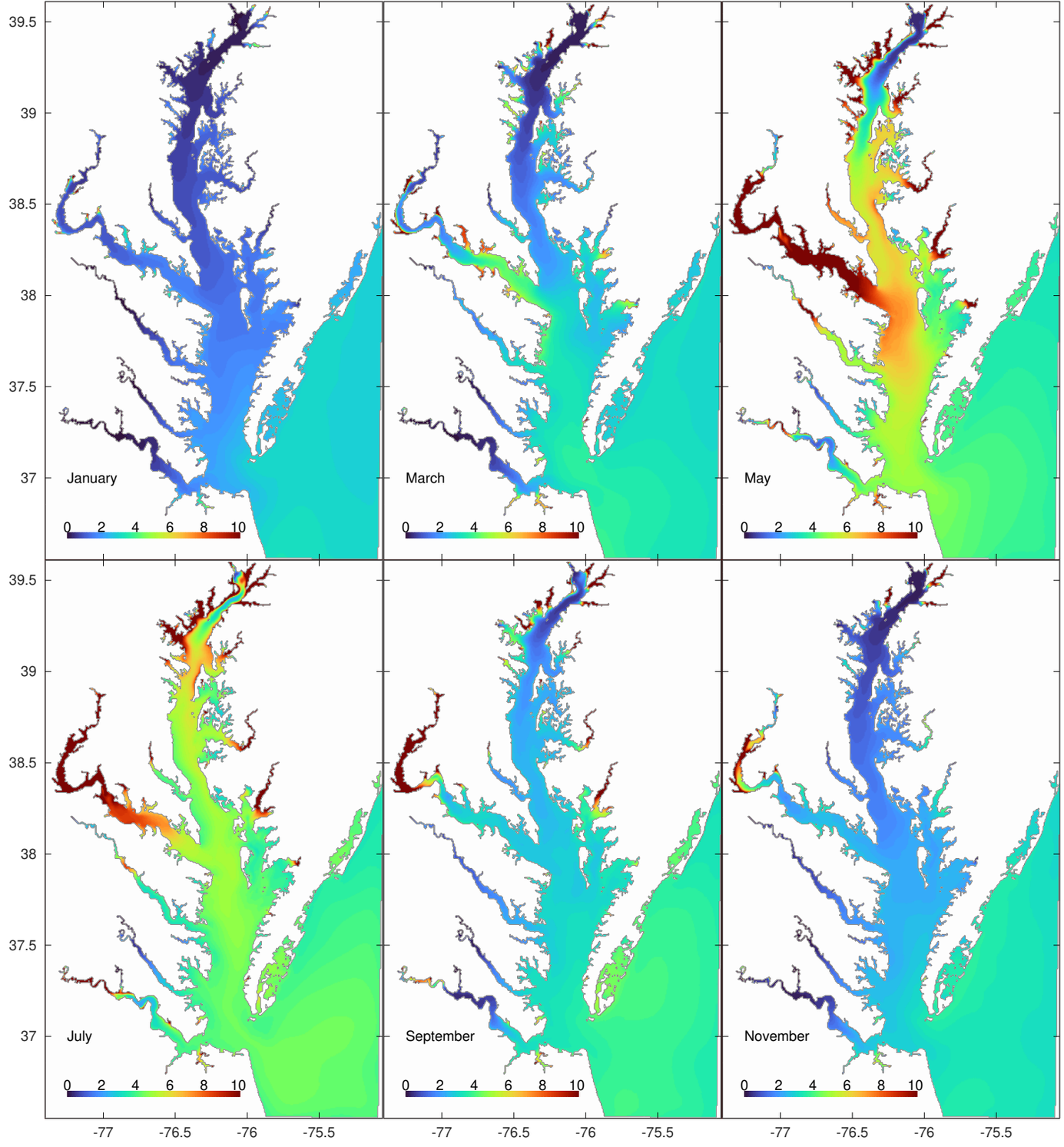

Figure 42: Calcite saturation state (Ω_{Ca}) at the surface.

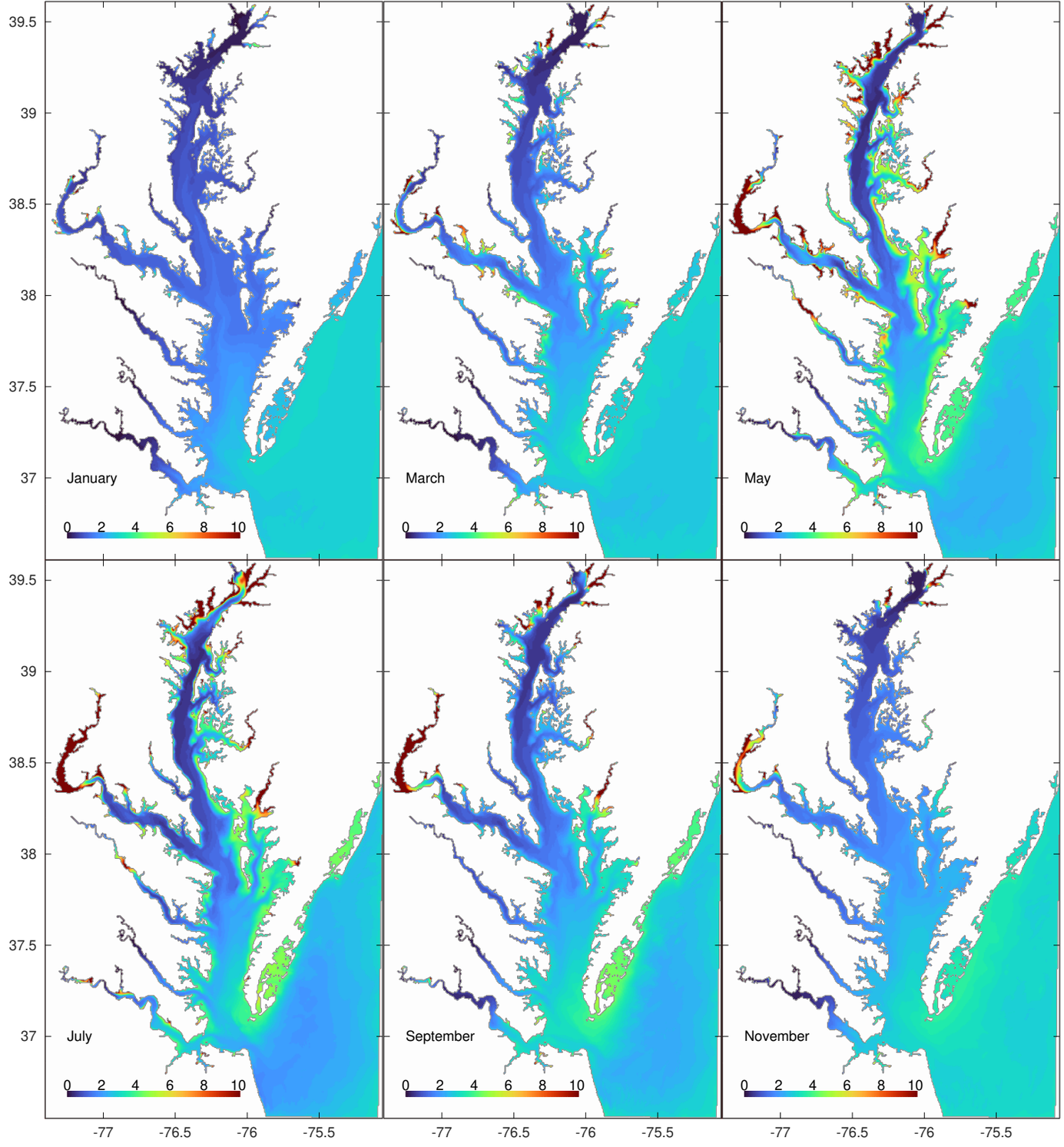

Figure 43: Calcite saturation state (Ω_{Ca}) at the bottom.

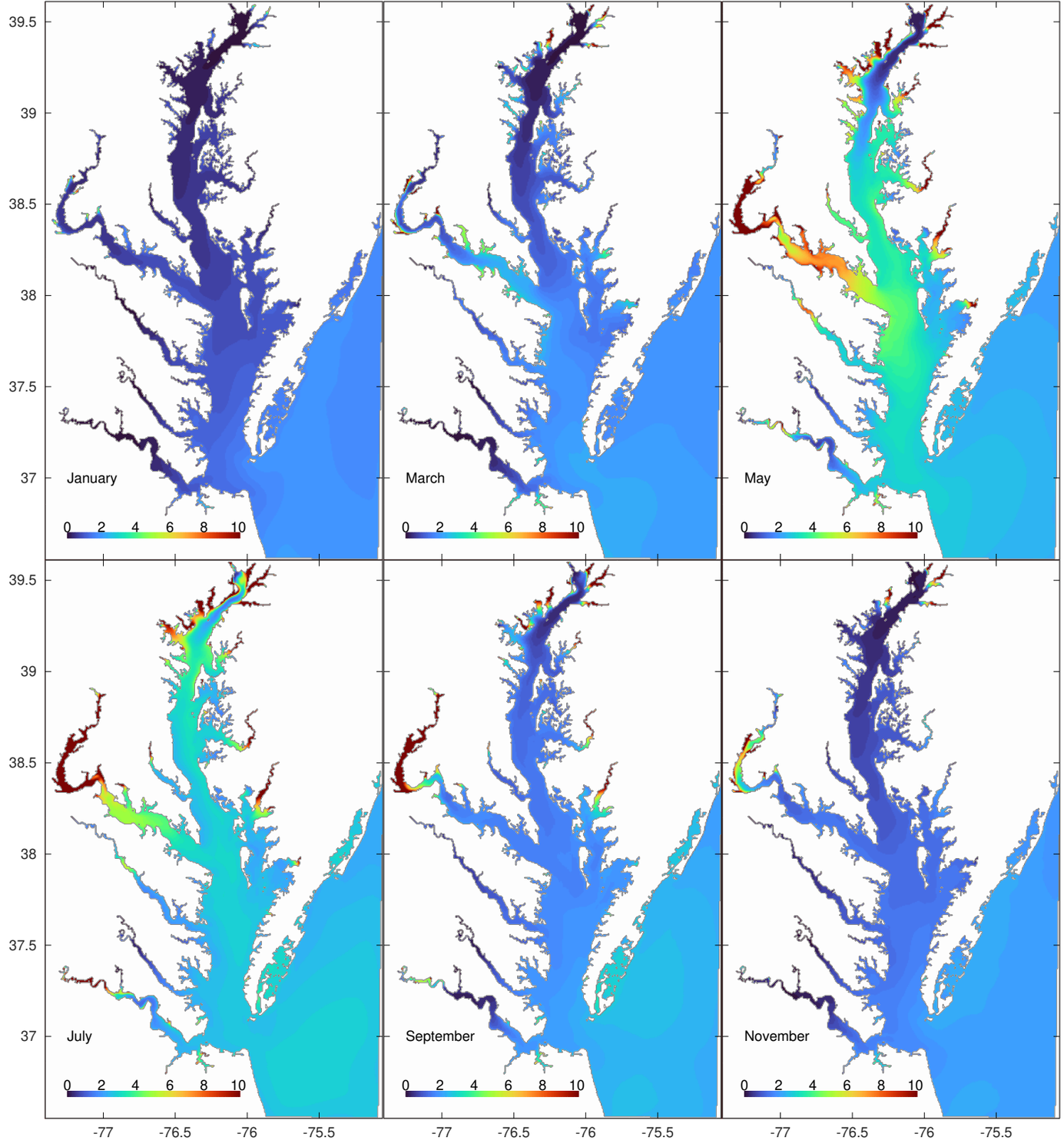

Figure 44: Aragonite saturation state (Ω_{Ar}) at the surface.

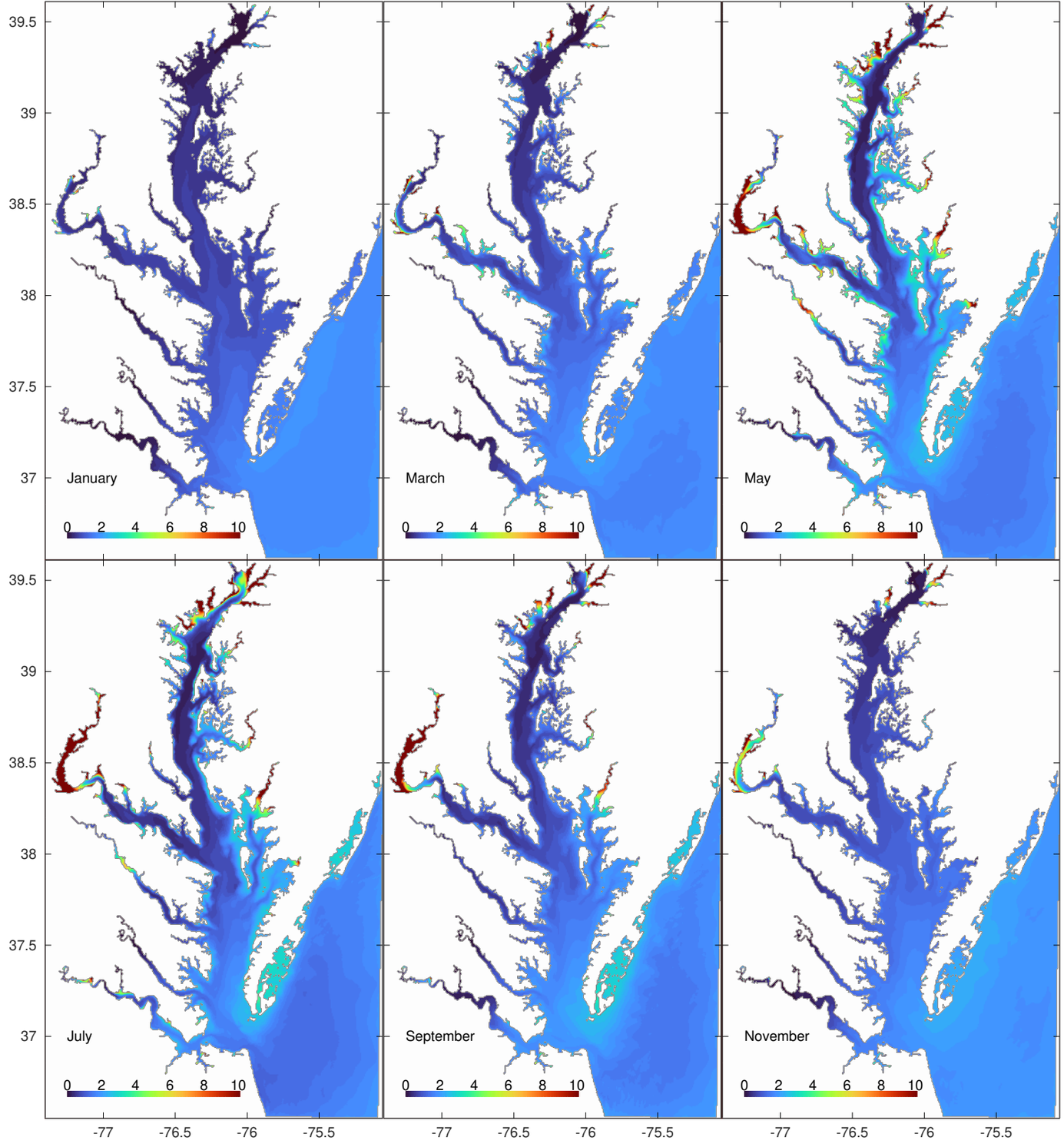

Figure 45: Aragonite saturation state (Ω_{Ar}) at the bottom.

(as a result of tidal motion and friction against the sea floor). The latter typically dominates in the Bay (note the change in scale between surface/bottom in Figs. 13–14).

Inorganic suspended solids (ISS) are computed by the model based on the equations of *Warner et al.* (2008). **Total suspended solids (TSS)** include both the inorganic component and an organic component computed by the biogeochemical module (Estuarine Carbon Biogeochemistry, ECB). **Diffuse light attenuation (K_d)** is derived using the equations of *Turner et al.* (2021) with coefficients updated to reflect the Bay as a whole (tributaries and main stem).

TA and **DIC** are the two state variables of the carbonate chemistry module in ECB. All other carbonate chemistry variables are derived from TA, DIC, temperature and salinity, notably **pH**, pCO_2 and **saturation states (Ω)**. This calculation uses CO2SYS (*van Heuven et al.*, 2011) except the saturation states which are computed with PyCO2SYS (*Humphreys et al.*, 2024) as the latter allows for calcium concentrations as an input. In both programs, the dissociation constants from *Cai and Wang* (1998) are used and concentrations of zero for silicate and phosphate are assumed for simplicity. Daily TA and DIC fields are used to compute daily pH, Ω and pCO_2, and these fields are then averaged over time to obtain the atlas climatology. **Calcium** is implemented in ROMS-ECB following *Westman et al.* (2023) and (in contrast to all other variables) is representative of a shorter period of years (2021–2023). Chlorophyll is not a state variable of ROMS-ECB and is therefore absent from the atlas. Nevertheless, it can be estimated from particulate organic carbon (POC) and diffuse light attenuation (K_d) using Eq. 15 from *Cerco and Noel* (2004).

4 Examples of usage

4.1 General tips on using the atlas

- Use the 'Zoom' function of your PDF viewer to visualize the details of the figures included in this documentation.

- You can create your own figures using the NetCDF file, *e.g.*, focus on specific sub-regions of the Bay, extract a monthly timeseries at specific locations, or even advect Lagrangian particles based on the climatological currents at the surface or bottom.

- Contact us to suggest additions or improvements. The atlas is a live document and new versions will be made available over time at the same `https://doi.org/` link.

4.2 QGIS / ArcGIS

The atlas corresponds to a library of georeferenced rasterized layers. For example, in QGIS, one would:

1. Select the tab `Layer`.
2. Select `Add Layer`.
3. Select `Add Raster Layer`.
4. Select the file `atlas_chesbay_vxxxxxxxx.nc` as the `Raster Dataset(s)`.
5. Select `Add`.
6. A window will open with a list of layers, each corresponding to a variable and a depth (surface or bottom). Select the layer of interest, for example, `salinity_bottom`.
7. The bottom salinity should be immediately visible as a geographical map with longitudes and latitudes. Each month of the climatology corresponds to a 'Band' representative of the center of the month (for a total of 12 bands).

4.3 Matlab / Octave

To visualize bottom salinity in the 6$^{\text{th}}$ month of the year (June):

1. `sbju = ncread( 'atlas_chesbay_vxxxxxxxx.nc', 'salinity_bottom' );`
2. `long = ncread( 'atlas_chesbay_vxxxxxxxx.nc', 'longitude'       );`
3. `lati = ncread( 'atlas_chesbay_vxxxxxxxx.nc', 'latitude'        );`
4. `imagesc([min(long),max(long)],[min(lati),max(lati)],squeeze(sbju(:,:,6))');`
5. `axis xy; axis equal; colorbar;`
6. The bottom salinity should be visible as a geographical map with longitudes and latitudes.

To obtain the June bottom salinity at an arbitrary location (76°W, 37.75°N):

1. `interp2( oreg, areg, squeeze( sbju(:, :, 6) )', -76, 37.75 )`

4.4 Python

To visualize bottom salinity in the 6th month of the year (June):

```
1. import netCDF4 as nc
2. import matplotlib.pyplot as plt
3. atla = nc.Dataset( 'atlas_chesbay_vxxxxxxxx.nc' )
4. sbju = atla.variables['salinity_bottom'][:]
5. fig, ax = plt.subplots()
6. ax.imshow(sbju[6,:,:])
7. plt.show()
```

5 About the 3-D numerical model (ROMS-ECB)

ROMS-ECB is an implementation of the Regional Ocean Modeling System (ROMS, *Shchepetkin and McWilliams*, 2005) designed for process-based studies of estuarine systems such as the Chesapeake Bay. It is a deterministic model based on biogeochemical processes ('mechanistic') and strictly enforcing conservation of volume, mass, heat, mechanical energy, nitrogen, carbon and dioxygen, throughout the model domain and at all times. These stringent requirements are necessary in process-based studies in order to quantitatively and unambiguously track the impact of a given process or perturbation in a reproducible and verifiable manner. These characteristics distinguish ROMS-ECB from *data-assimilative models* (where the requirements of conservation and deterministic behavior are abandoned in order to ingest available observations) or *forecast models* (where a close match to available observations is the sole requirement). Despite these constraints, the vast suite of historical data available in the Chesapeake Bay allowed for a careful calibration of ROMS-ECB and permit the model to generate reasonable predictions for a large ensemble of environmental variables (see §6 for an evaluation of ROMS-ECB).

The ECB module is an evolution of *Fasham et al.* (1990) with various components added over the years (while remaining close to the original goals of parsimony and tractability). Sediment denitrification was implemented by *Fennel et al.* (2006) followed by carbonate chemistry (*Fennel et al.*, 2008). *Druon et al.* (2010) implemented bottom resuspension, burial and dissolved organic matter. *Feng et al.* (2015) introduced the ECB acronym and implemented water-column denitrification. *Da et al.* (2018) implemented temperature dependence for most biogeochemical processes as well as atmospheric nitrogen deposition. *Turner et al.* (2021) introduced the dynamic sediment module of *Warner et al.* (2008) and inputs from shoreline erosion. *St-Laurent and Friedrichs* (2024) implemented a finer computational grid of 600 m as well as the wetting-drying scheme of *Warner et al.* (2013). A detailed documentation of the equations of ECB is available in the supporting information of *St-Laurent et al.* (2020) while the code is archived in *St-Laurent and Friedrichs* (2023).

The atmospheric forcing of the 1985–2023 hindcast is based on the ERA5 reanalysis (*Hersbach et al.*, 2023) while physical air-sea fluxes are computed every time-step (60 s) following *Fairall et al.* (2003). Air-sea fluxes of dioxygen and carbon dioxide are calculated every time-step (*Wanninkhof*, 2014). Atmospheric deposition of nitrogen follows *Da et al.* (2018). Over the portion 1985–2020 of the 1985–2023 hindcast, terrestrial inputs (which include the contribution from groundwater discharge and shorelines) are taken from Phase 6 IndicatorC19Ext2020 (*Bhatt et al.*, 2023). These daily terrestrial loadings are distributed across ECB's state variables following *Irby and Friedrichs* (2019) and aggregated into 95 input points positioned across the Bay. DIC and TA concentrations associated with these terrestrial inputs are based on historical analyses by the USGS as described in *Da et al.* (2021). Over the portion 2021–2023 of the 1985–2023 hindcast, the terrestrial inputs combine observed freshwater discharges scaled up to represent the full Chesapeake watershed (*Bever et al.*, 2021) as well as concentrations from a neural network analysis of the earlier 1985–2020 period (A. Bever, AnchorQEA). Wind wave conditions at 3-hourly frequency were computed using SWAN (*Booij et al.*, 1996) and atmospheric conditions from ERA5 (A. Bever, AnchorQEA). The 37 tidal constituents from *Szpilka et al.* (2016) are combined with 4-hourly detided water levels observed at Lewes DE and Duck NC and prescribed at the shelf boundary (note that historical sea level rise is intrinsic to these observed water levels). Practical salinity and potential temperature at this boundary correspond to seasonal climatologies (*Boyer et al.*, 2018) assumed to be representative of year 2013 and supplemented by long-term linear trends following *Da et al.* (2021). Conditions along the shelf boundary also include climatologies for nitrate (*Boyer et al.*, 2018), DOC (*Mannino et al.*, 2016), DON,PON,POC,ammonium (*Filippino et al.*, 2011), TA and DIC (supplemented by a long-term linear trend for DIC:TA; see *Da et al.* (2021)). Dioxygen concentrations along the shelf boundary are computed from temperature and salinity and assumed to be at saturation.

The hindcast simulation on which the atlas is based was conducted at the Virginia Institute of Marine Science (VIMS) between 2024-01-08 and 2024-03-16 (runs 830, 833, 847, 857, 864, 876, 883, 889, 896, 911, 921, 927, 935, 947–962, 964–966, 968–974) on the high-performance cluster 'James'.

6 Evaluation of model skill

Historical data corresponding to the period of the hindcast simulation are used to evaluate the model skill. The majority of the data originates from the Water Quality Monitoring Program (WQMP, *USEPA*, 2023) initiated in 1984 and continuing to this day, but the spatial and temporal coverage of the data varies widely across variables. Temperature, salinity and dissolved O_2 have the best coverage while variables such as fixed suspended solids often have major gaps in time and/or were limited to a few specific tributaries. In all cases, the results from the hindcast simulation were sampled at the same location, depth, and time as the historical data and paired with the measurement for comparison.

Each figure provides a scatterplot of the model-data pairs, or more specifically the relative distribution of those pairs within the space represented in the figure. This relative distribution is obtained by discretizing the space into a 25×25 grid and computing the number of pairs falling within each grid cell. For example, the bottom-left grid cell in the salinity scatterplot (Fig. 46) represents pairs falling in the range $0 \leq S < 1.4$. This density distribution is contoured with a linear color shading ranging from zero (white) to the maximum density value (dark blue). Note that the contouring begins at the center of the first grid cell, *i.e.* at $S = 0.7$ in the example of Fig. 46. This visualization is superior to a traditional scatter plot in cases where the number of pairs is large, and also has the benefit of highlighting the relative distribution of the measurements across the possible range of values. Note that the spatio-temporal sampling of the WQMP often favors a specific segment in the range of possible values, *e.g.* warm temperatures in Fig. 46 reflecting more frequent sampling in the summer months. An ideal match between model and data would correspond to high densities along the 1:1 line.

The figures are accompanied with statistics: number of model-data pairs (N), first/last years of data used, arithmetic average of the measurements (Mean obs.), standard deviation of the measurements (STD obs.), model bias ($Mean\_model - Mean\_obs$), Spearman rank correlation, coefficient of determination ($R^2 = 1 - residual\_sum\_squares \div total\_sum\_squares$), linear regression $y = ax + b$, and unbiased root mean squared deviation (*Jolliff et al.*, 2009). The model skill is generally highest for physical fields (temperature and salinity) and gradually worsens for dissolved inorganic substances, dissolved organic matter, and finally particulate matter given its dependence on resuspension and vertical settling.

Fixed suspended solids (**FSS**) data are from the WQMP database and can be viewed as our best observational proxy for inorganic suspended solid concentrations in tidal water. FSS includes an organic component which is estimated following *Turner et al.* (2021). Only FSS data from 2002 onward are used as the spatial coverage was too poor previously (same for $\mathbf{K_d}$). Only **pH** data from 1996 onward are used as this variable previously had a bias in Virginia water (*Da et al.*, 2021). Climate quality **TA** and **DIC** are not available from the WQMP and thus this model evaluation relies on the Bay-wide data of *Friedman et al.* (2020).

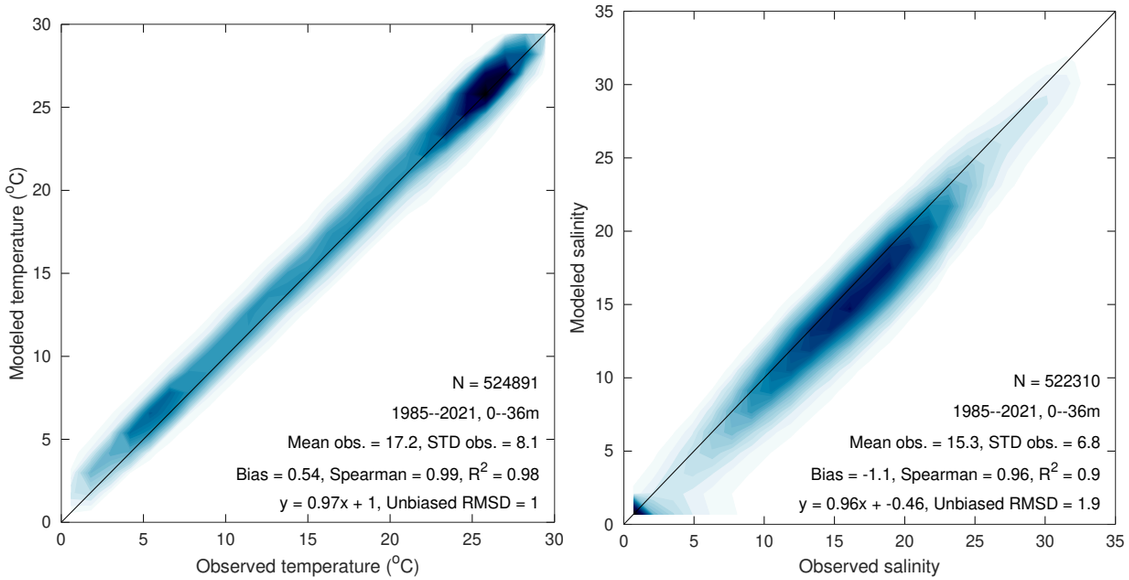

Figure 46: Evaluation of model skill against historical observations.

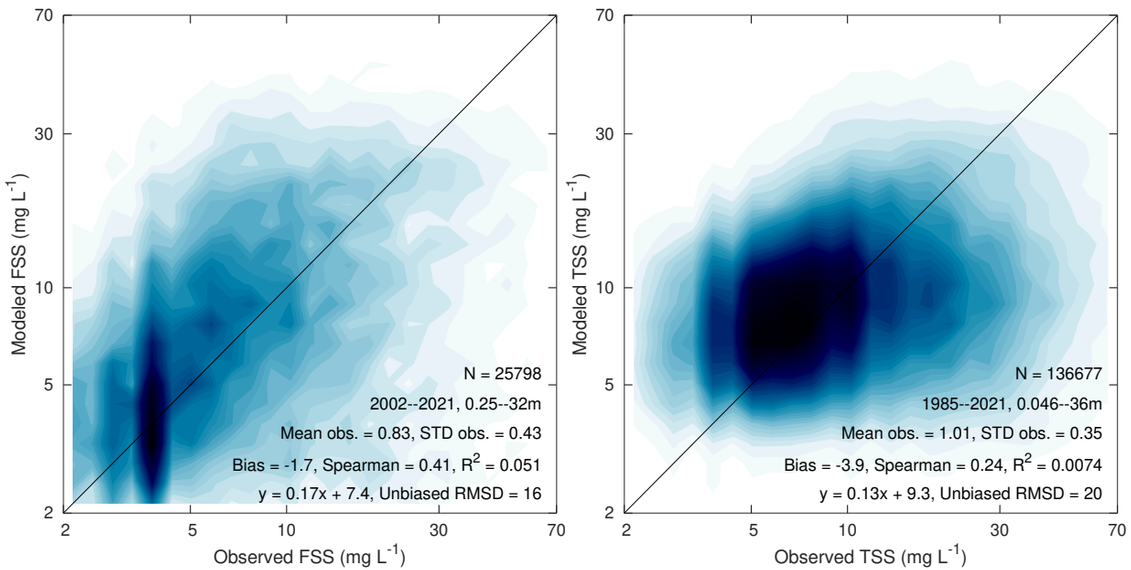

Figure 47: Evaluation of model skill against historical observations (continued).

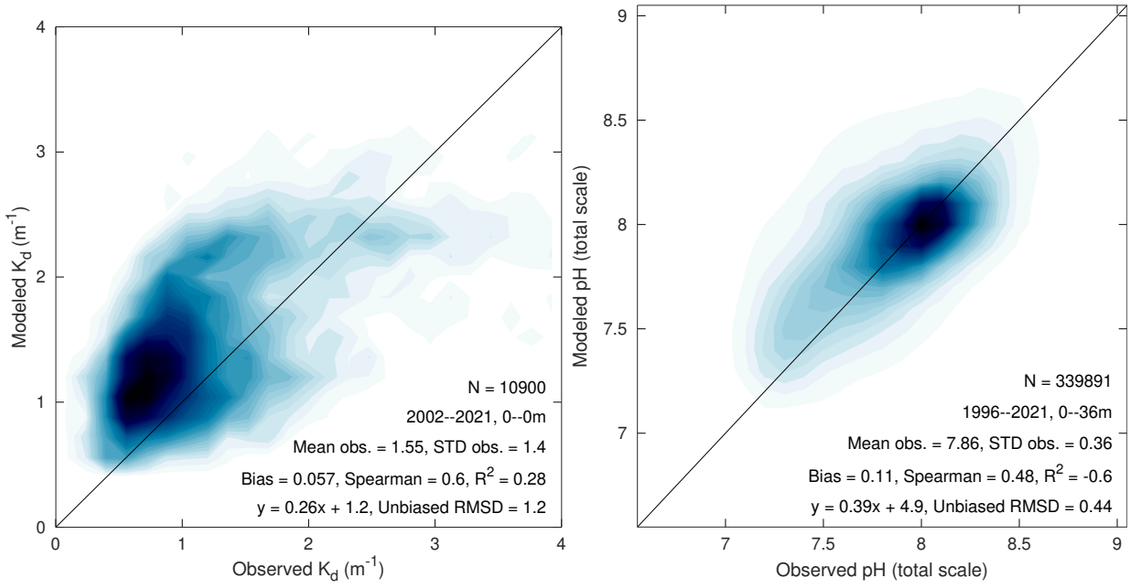

Figure 48: Evaluation of model skill against historical observations (continued).

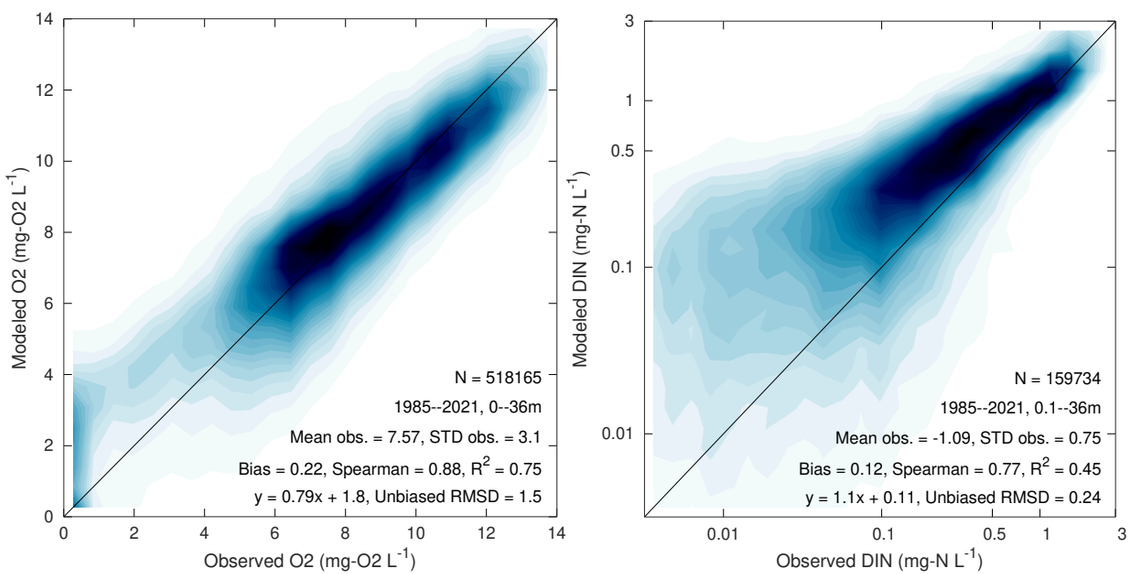

Figure 49: Evaluation of model skill against historical observations (continued).

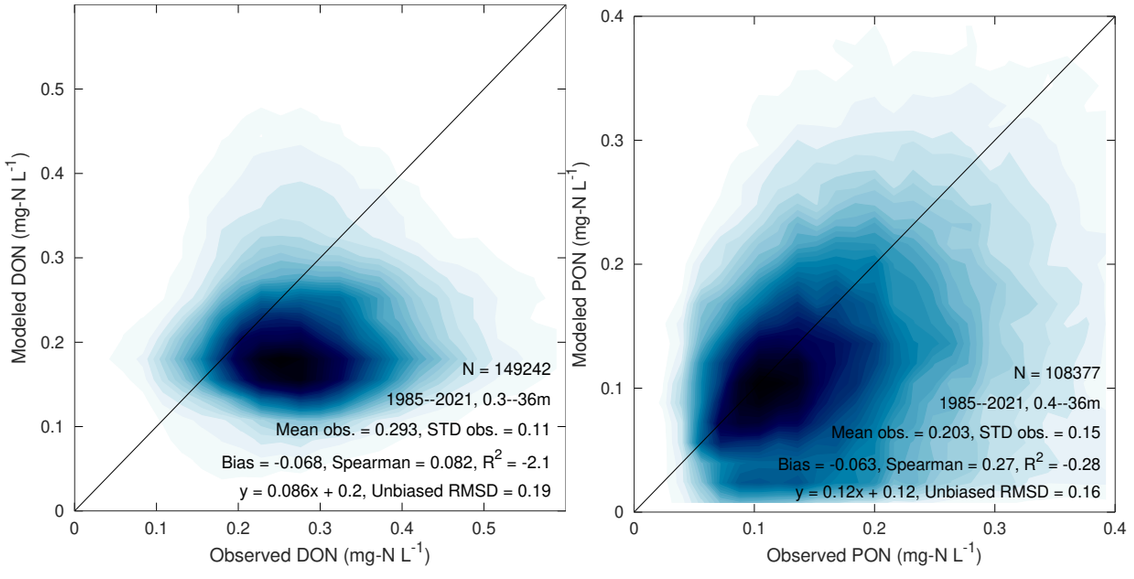

Figure 50: Evaluation of model skill against historical observations (continued).

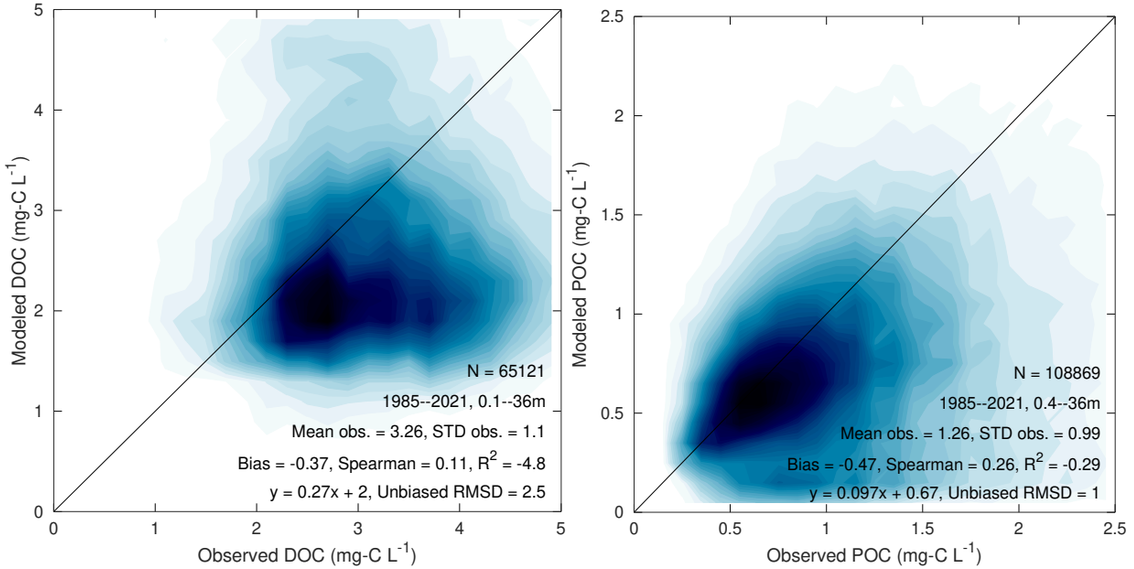

Figure 51: Evaluation of model skill against historical observations (continued).

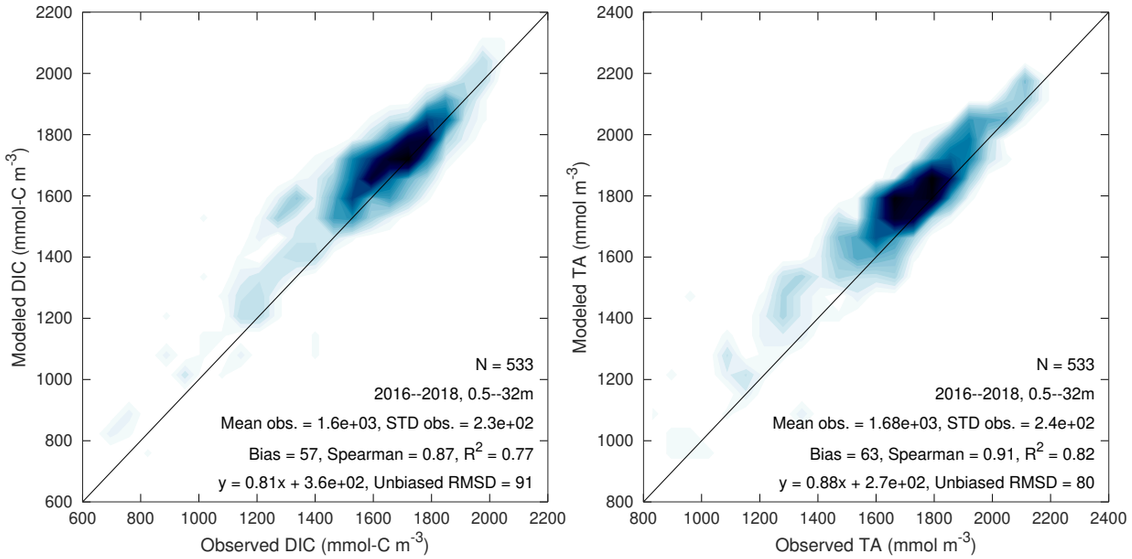

Figure 52: Evaluation of model skill against historical observations (continued).

7 Acknowledgments

This work was supported by the National Science Foundation (collaborative award 2148952), the Mid-Atlantic Regional Association Coastal Observing System (MARACOOS; NOAA NA21NOS0120096) as well as the National Oceanic and Atmospheric Administration (NOAA) under awards NA23NMF4570426, NA23NOS4780289, NOAA-NOS-IOOS-2021-2006729, and NA20OAR0170473. The authors acknowledge William & Mary Research Computing (`https://www.wm.edu/it/rc`) for providing computational resources and/or technical support that have contributed to the results reported within this report. Gopal Bhatt (The Pennsylvania State University, US EPA Chesapeak Bay Program Office) provided terrestrial inputs from Phase 6 for the period 1985–2020. Aaron Bever (AnchorQEA) provided wind wave conditions for 1985–2023 as well as terrestrial inputs for 2021–2023. Edward G. Stets (USGS) provided timeseries of DIC and TA for multiple tributaries of the Chesapeake Bay.

References

Bever, A. J., M. A. M. Friedrichs, and P. St-Laurent (2021), Real-time environmental forecasts of the Chesapeake Bay: Model setup, improvements, and online visualization, *Environmental Modelling and Software*, *140*, doi:10.1016/j.envsoft.2021.105036.

Bhatt, G., L. Linker, G. Shenk, I. Bertani, R. Tian, J. Rigelman, K. Hinson, and P. Claggett (2023), Water quality impacts of climate change, land use, and population growth in the Chesapeake Bay watershed, *Journal of the American Water Resources Association*, pp. 1–29, doi:10.1111/1752-1688.13144.

Booij, N., L. H. Holthuijsen, and R. C. Ris (1996), The "SWAN" wave model for shallow water, in *Coastal Engineering 1996*, edited by B. L. Edge, American Society of Civil Engineers, doi:10.1061/9780784402429.053.

Boyer, T. P., H. E. Garcia, R. A. Locarnini, M. M. Zweng, A. V. Mishonov, J. R. Reagan, K. A. Weathers, O. K. Baranova, D. Seidov, and I. V. Smolyar (2018), World Ocean Atlas 2018: temperature and salinity.

Cai, W. J., and Y. Wang (1998), The chemistry, fluxes, and sources of carbon dioxide in the estuarine waters of the Satilla and Altamaha Rivers, Georgia, *Limnol. Oceanogr.*, *43*(4), 657–668.

Cerco, C. F., and M. R. Noel (2004), Process-based primary production modeling in Chesapeake Bay, *Marine Ecology Progress Series*, *282*, 45–58.

Da, F., M. A. M. Friedrichs, and P. St-Laurent (2018), Impacts of atmospheric nitrogen deposition and coastal nitrogen fluxes on oxygen concentrations in Chesapeake Bay, *J. Geophys. Res.: Oceans*, *123*, 5004–5025, doi:10.1029/2018jc014009.

Da, F., M. A. M. Friedrichs, P. St-Laurent, E. Shadwick, R. Najjar, and K. Hinson (2021), Mechanisms driving decadal changes in the carbonate system of a coastal plain estuary, *J. Geophys. Res. Oceans*, *126*(e2021JC017239), doi:10.1029/2021JC017239.

Druon, J., A. Mannino, S. Signorini, C. McClain, M. A. M. Friedrichs, J. Wilkin, and K. Fennel (2010), Modeling the dynamics and export of dissolved organic matter in the Northeastern US continental shelf, *Estuarine Coastal and Shelf Science*, *88*(4), 488–507, doi:10.1016/j.ecss.2010.05.010.

Fairall, C. W., E. F. Bradley, J. E. Hare, A. A. Grachev, and J. B. Edson (2003), Bulk parameterization of air-sea fluxes: Updates and verification for the COARE algorithm, *J. Clim.*, *16*, 571–591.

Fasham, M. J. R., H. W. Ducklow, and S. M. McKelvie (1990), A nitrogen-based model of plankton dynamics in the oceanic mixed layer, *J. Mar. Res.*, *48*, 591–639.

Feng, Y., M. A. M. Friedrichs, J. Wilkin, H. Tian, Q. Yang, E. E. Hofmann, J. D. Wiggert, and R. R. Hood (2015), Chesapeake bay nitrogen fluxes derived from a land-estuarine ocean

biogeochemical modeling system: Model description, evaluation, and nitrogen budgets, *J. Geophys. Res. Biogeosciences*, *120*(8), 1666–1695, doi:10.1002/2015JG002931.

Fennel, K., J. Wilkin, J. Levin, J. Moisan, J. O'Reilly, and D. Haidvogel (2006), Nitrogen cycling in the Middle Atlantic Bight: Results from a three-dimensional model and implications for the North Atlantic nitrogen budget, *Global Biogeochemical Cycles*, *20*(GB3007), doi:10.1029/2005GB002456.

Fennel, K., J. Wilkin, M. Previdi, and R. Najjar (2008), Denitrification effects on air-sea CO_2 flux in the coastal ocean: Simulations for the northwest North Atlantic, *Geophys. Res. Lett.*, *35*(24), doi:10.1029/2008gl036147.

Filippino, K. C., M. R. Mulholland, and P. W. Bernhardt (2011), Nitrogen uptake and primary productivity rates in the Mid-Atlantic Bight (MAB), *Estuarine, Coastal and Shelf Science*, *91*, 13–23, doi:10.1016/j.ecss.2010.10.001.

Forte, M. F., J. L. Hanson, L. Stillwell, M. Blanchard-Montgomery, B. Blanton, R. Luettich, H. Roberts, J. Atkinson, and J. Miller (2011), FEMA region III storm sturge study: Coastal storm surge analysis system digital elevation model, Coastal and Hydraulics Laboratory, ERDC/CHL TR-11-1, US Army Corps of Engineers, Engineer Research and Development Center.

Friedman, J. R., E. H. Shadwick, M. A. M. Friedrichs, R. G. Najjar, O. A. De Meo, F. Da, and J. L. Smith (2020), Seasonal variability of the CO_2 system in a large coastal plain estuary, *J. Geophys. Res.: Oceans*, *125*(1), e2019JC015,609, doi:10.1029/2019JC015609.

Hersbach, H., B. Bell, P. Berrisford, G. Biavati, A. Horanyi, J. M. Sabater, J. Nicolas, C. Peubey, R. Radu, I. Rozum, D. Schepers, A. Simmons, C. Soci, D. Dee, and J. N. Thepaut (2023), ERA5 hourly data on single levels from 1940 to present, doi:10.24381/cds.adbb2d47.

Humphreys, M. P., A. J. Schiller, D. E. Sandborn, L. Gregor, D. Pierrot, S. M. A. C. van Heuven, E. R. Lewis, and D. W. R. Wallace (2024), PyCO2SYS: marine carbonate system calculations in Python, Zenodo, doi:10.5281/zenodo.3744275.

Irby, I. D., and M. A. M. Friedrichs (2019), Evaluating confidence in the impact of regulatory nutrient reduction on Chesapeake Bay water quality, *Estuaries and Coasts*, *42*, 16–32, doi:10.1007/s12237-018-0440-5.

Jolliff, J. K., J. C. Kindle, I. Shulman, B. Penta, M. A. M. Friedrichs, R. Helber, and R. A. Arnone (2009), Summary diagrams for coupled hydrodynamic-ecosystem model skill assessment, *J. Mar. Syst.*, *76*, 64–82, doi:10.1016/j.jmarsys.2008.05.014.

Mannino, A., S. R. Signorini, M. G. Novak, J. Wilkin, M. A. M. Friedrichs, and R. G. Najjar (2016), Dissolved organic carbon fluxes in the Middle Atlantic Bight: An integrated approach based on satellite data and ocean model products, *J. Geophys. Res.: Biogeosciences*, *121*, doi:10.1002/2015JG003031.

National Geophysical Data Center (1999), 3 arc-seconds Coastal Relief Model (CRM) volume 2 (southeast Atlantic), file crm_vol2.nc, NOAA, accessed 2019-05-08, doi:10.7289/V53R0QR5.

NOAA (2022), Estuarine bathymetric digital elevation models, NCEI, https://www.ngdc.noaa.gov/mgg/bathymetry/estuarine/index.html, accessed 2022-11-02.

Parker, B. B. (2007), Tidal analysis and prediction, *Tech. rep.*, NOAA Special Publication NOS CO-OPS 3, Silver Spring, Maryland.

Pope, J. P., D. C. Andreasen, E. R. McFarland, and M. K. Watt (2016), Digital elevations and extents of regional hydrogeologic units in the northern Atlantic coastal plain aquifer system from Long Island, New York, to North Carolina, U.S. Geological Survey data release, accessed 2020-09-01, doi:10.5066/F70V89WN.

Shchepetkin, A. F., and J. C. McWilliams (2005), The Regional Oceanic Modeling System (ROMS): A split-explicit, free-surface, topography-following-coordinate oceanic model, *Ocean Model.*, *9*, 347–404, doi:10.1016/j.ocemod.2004.08.002.

St-Laurent, P., and M. A. M. Friedrichs (2023), Dataset: Numerical experiments on the sensitivity of Chesapeake Bay hypoxia to physical forcings and the associated code and input files (32 gigabytes), doi:10.25773/q2kh-rd09.

St-Laurent, P., and M. A. M. Friedrichs (2024), On the sensitivity of coastal hypoxia to its external physical forcings, *J. Adv. Model. Earth Syst.*, *16*(e2023MS003845), doi:10.1029/2023MS003845.

St-Laurent, P., M. A. M. Friedrichs, R. G. Najjar, E. H. Shadwick, H. Tian, and Y. Yao (2020), Relative impacts of global changes and regional watershed changes on the inorganic carbon balance of the Chesapeake Bay, *Biogeosciences*, *17*, 3779–3796, doi:10.5194/bg-17-3779-2020.

Szpilka, C., K. Dresback, R. Kolar, J. Feyen, and J. Wang (2016), Improvements for the western North Atlantic, Caribbean and Gulf of Mexico ADCIRC tidal database (EC2015), *J. Mar. Sci. Eng.*, *4*(72), doi:10.3390/jmse4040072.

Turner, J. S., P. St-Laurent, M. A. M. Friedrichs, and C. T. Friedrichs (2021), Effects of reduced shoreline erosion on Chesapeake Bay water clarity, *Science of the total environment*, *769*(145157), doi:10.1016/j.scitotenv.2021.145157.

USEPA (2023), CBP water quality database (1984-present), U.S. Environmental Protection Agency, Chesapeake Bay Program Office, https://www.chesapeakebay.net/what/downloads/cbp-water-quality-database-1984-present.

van Heuven, S., D. Pierrot, J. W. B. Rae, E. Lewis, and D. W. R. Wallace (2011), MATLAB program developed for CO_2 system calculations, ORNL/CDIAC-105b, *Tech. rep.*, Oak Ridge, Tennessee: Carbon Dioxide Information Analysis Center, Oak Ridge National Laboratory, U.S. Department of Energy.

Wanninkhof, R. (2014), Relationship between wind speed and gas exchange over the ocean revisited, *Limnology and oceanography: Methods*, *12*, 351–362, doi:10.4319/lom.2014.12.351.

Warner, J., C. Sherwood, H. Arango, and R. Signell (2005), Performance of four turbulence closure models implemented using a generic length scale method, *Ocean Modelling*, *8*, 81–113, doi:10.1016/j.ocemod.2003.12.003.

Warner, J. C., C. R. Sherwood, R. P. Signell, C. K. Harris, and H. G. Arango (2008), Development of a three-dimensional, regional, coupled wave, current, and sediment-transport model, *Computers & Geosciences*, *34*, 1284–1306, doi:10.1016/j.cageo.2008.02.012.

Warner, J. C., Z. Defne, K. Haas, and H. G. Arango (2013), A wetting and drying scheme for ROMS, *Computers & Geosciences*, *58*, 54–61, doi:10.1016/j.cageo.2013.05.004.

Westman, R., B. Stewart, D. Kerins, R. Najjar, L. Li, and E. G. Stets (2023), Influence of watershed characteristics and warming on stream chemistry, *Tech. rep.*, Research Experience for Undergraduates (REU) report, The Pennsylvania State University, The Pennsylvania State University.

Ye, F., Y. J. Zhang, H. V. Wang, M. A. M. Friedrichs, I. D. Irby, A. Valle-Levinson, Z. Wang, H. Huang, J. Shen, and J. Du (2017), Assessment of a 3D unstructured-grid model for the Chesapeake Bay and adjacent shelf: Supplementary materials, William & Mary Scholarworks, accessed 2021-04-26, doi:10.21220/V5HK5S.